INTERNATIONAL JOURNAL FOR NUMERICAL METHODS IN FLUIDS
Int. J. Numer. Meth. Fluids 2003; **43**:431–462 (DOI: 10.1002/fld.613)

A deconvolution-based fourth-order finite volume method for incompressible flows on non-uniform grids

P. Iannelli[1,2], F. M. Denaro[1,*,†] and G. De Stefano[1]

[1] *Dipartimento di Ingegneria Aerospaziale e Meccanica, Seconda Universita' degli Studi di Napoli, Italy*
[2] *Present Address: Centro Italiano Ricerche Aerospaziali, Capua, Italy*

SUMMARY

This paper is concerned with the development of a new high-order finite volume method for the numerical simulation of highly convective unsteady incompressible flows on non-uniform grids. Specifically, both a high-order fluxes integration and the implicit deconvolution of the volume-averaged field are considered. This way, the numerical solution effectively stands for a fourth-order approximation of the point-wise one. Moreover, the procedure is developed in the framework of a projection method for the pressure–velocity decoupling, while originally deriving proper high-order intermediate boundary conditions. The entire numerical procedure is discussed in detail, giving particular attention to the consistent discretization of the deconvolution operation. The present method is also cast in the framework of approximate deconvolution modelling for large-eddy simulation. The overall high accuracy of the method, both in time and space, is demonstrated. Finally, as a model of real flow computation, a two-dimensional time-evolving mixing layer is simulated, with and without sub-grid scales modelling.

KEY WORDS: high order finite volumes schemes; non-uniform grids fractional time-step method; approximate deconvolution large eddy simulation

1. INTRODUCTION

Numerical simulations of highly convective unsteady flows demand accurate numerical schemes in order to properly resolve the wide range of the time and length scales involved. Traditionally, the Navier–Stokes (NS) equations have been discretized on staggered grid with second-order accurate central finite difference (FD) schemes (e.g. References [1, 2]). The use of such schemes becomes particularly critical in large-eddy simulation (LES) where the unknown sub-grid scale (SGS) stresses must be modelled in terms of the resolved field. In fact, the highest wave number components could be strongly contaminated by large numerical errors associated with low order methods. Hence, much more attention has been recently devoted to the correlation between numerical and modelling errors (e.g. References [3, 4]).

*Correspondence to: F. M. Denaro, Dipartimento di Ingegneria Aerospaziale e Meccanica, Real Casa dell' Annunziata, Via Roma 29, 81031, Aversa (CE), Italy.
†E-mail: denaro@unina.it

Received 17 December 2002
Revised 27 May 2003

In particular, the second-order spatial accuracy was theoretically demonstrated to be too poor for computing an accurate LES solution. Nevertheless, for a long time, the use of second-order FD schemes has been the standard in LES of turbulent flows and this kind of discretization was recognized to be related to the implicit application of volume-averaging (e.g. Reference [5]). Moreover, second-order FD methods have been used for performing LES on non-uniform grids without taking into account the lack of commutativity between non-homogeneous averaging and differentiation. The commutation error terms arising from second-order schemes result of the same magnitude order of the local truncation error and the correct LES equations were analysed in Reference [6]. Thus, various forms of higher-order FD schemes for both staggered and co-located non-uniform grids have been applied. For instance, in References [7–10] the main issue consisted in developing appropriate discrete operators in order to get high-spatial accuracy, while respecting both the conservation of balanced quantities and the symmetry of the differential operators (i.e. preserving the fundamental properties of the continuum model).

On the other hand, the integral formulation of the NS equations is on the basis of the finite volume (FV) methods, representing discrete models which allow the balanced quantities, i.e. mass and momentum, to be *a priori* conserved. However, the kinetic energy is not automatically conserved in the inviscid limit and special schemes should be constructed to ensure discrete energy conservation [7, 8]. Therefore, although the integral form is more difficult to discretize than the differential counterpart, it appears to be the most natural from a physical point of view. Before introducing the concept of high-order FV methods, it is necessary to emphasize a fundamental difference between FV and FD approximations as it concerns their accuracy. By definition, a FD method is of accuracy order p if the *local truncation error*, that is the difference between the discrete and the differential operators applied onto the exact solution, is $O(h^p)$, h being the grid spacing [11]. As a matter of fact, for practical purposes, one usually can measure the accuracy by evaluating, for vanishing grid spacing, the asymptotic behaviour of the *discretization error*, that is the difference between the numerical solution and a reference one (possibly, under conditions of existence and uniqueness, the exact solution, e.g. Reference [12]).

In FV formulations, one approximates the flux integrals by means of a numerical flux function, obtaining the numerical solution in terms of a volume-averaged field, and higher order methods are constructed by increasing the spatial accuracy for fluxes approximation. It is important to note how the development of such methods has been strongly influenced by the research on numerical simulation of compressible inviscid flows (e.g. References [13, 14]). In this case, the integral formulation remains the only one mathematically admissible and, from the well-known Lax-Wendroff theorem, if the FV solution converges it does so toward a physical solution of the conservation law, namely the so-called *weak* solution (e.g. Reference [11]).

Conversely, for incompressible viscous flows simulation, where regular solutions are somehow expected, it makes sense to seek for higher-order point-wise solutions than the volume-averaged one. A fourth-order procedure, based upon Lagrangian interpolation, was developed for solving steady incompressible flows by using a co-located variable arrangement in Reference [15], while a compact fourth-order FV method, based upon the Padé approximation for the flux integration and a fully coupled velocity–pressure methodology, was recently presented in Reference [16]. In the latter paper, a deconvolution procedure was proposed as a post-processing tool for plotting a more detailed velocity field. As the deconvolution is

performed after the computation of the flow field is finished, it does not enter into the dynamics of the resolved cell-averaged velocity.

In this paper, a high-order FV methodology in which the time-dependent solution is a self-representation of a high-order discrete approximation to the point-wise solution, the deconvolution procedure being built-in in the adopted numerical formulation, is proposed. Following a series of papers on a local average method, introduced and developed in References [17–19], the present numerical procedure is based on the approximate deconvolution of the integral NS equations. Hence, starting from the classical top-hat filtering procedure, a class of high-order filters is defined. The introduction of higher-order filtered variables is very attractive for turbulence modelling. In fact, the present method can be also viewed in the framework of the so-called *implicit structural models* for LES, as discussed in Reference [20]. In particular, it was demonstrated in Reference [19] how, by increasing the de-averaging order, the high-order filtered variable tends toward the spectral cut-off filtered counterpart, which is more appealing from the physical point of view [21–23]. However, since sharp cut-off filtering is naturally related to spectral methods, which are limited to simulations of simple geometry flows, more complex flows can be conveniently treated by means of FV methods. Furthermore, non-uniform computational grids are necessary in handling non-homogeneous flows, even for simple geometry.

Therefore, one of the aims of this study is to extend this high-order filtering methodology to more general problems than those manageable by spectral methods. Following these guidelines, a real fourth-order FV method for unsteady flows on non-uniform grids, based on a fractional time-step (FTS) method for the velocity–pressure decoupling (e.g. References [24–26]), is constructed. In considering the governing equations for the high-order filtered velocity, as the integral and differential operators do not commute for non-uniform grids, either additional terms should be computed or special filtering should be adopted [6, 23, 27]. An original strategy for avoiding the explicit computation of the above-mentioned additional terms is proposed, which consists in resolving a modified momentum equation, wherein the approximate inverse deconvolution is applied directly upon the velocity time derivative. Note that, when solving the unsteady NS equations by means of the FV approach, the time derivative involves the cell-averaged velocity. For second-order methods, the latter is congruently approximated by the cell value at the cell circum-centre whereas, for higher order methods, a coupling between the cell value to its neighbouring nodes becomes necessary. This operation is usually referred to as reconstruction or, according to the Finite Element literature, mass matrix construction [28] and strongly depends on the assumption about the underlying functional form of the solution. The present reconstruction procedure based upon the truncated Taylor series expansion is here preferred as it can be interpreted in terms of a differential de-filtering operation in the LES approach (e.g. Reference [20]).

As far as the spatial discretization is concerned, the flux integration is congruently performed to fourth-order accuracy, by adopting both the Simpson integration formula and the Lagrange polynomial interpolation on Cartesian non-uniform grids. In order to simplify the procedure, it has been decided to co-locate the variables at the same grid nodes, rather than to adopt a staggered grid. However, owing to the strong even–odd coupling associated with the adopted stencil, no spurious pressure solutions were produced. Eventually, by adopting the second-order semi-implicit Adams-Bashforth/Crank-Nicolson (AB/CN) scheme, the time integration of the governing equations was carried out. It is worth noting how, in order to obtain a time-accurate solution, a careful definition of the intermediate boundary conditions for the FTS

method is required [25, 26, 29, 30]. In the present paper, an original methodology for deriving congruent second-order time-accurate boundary conditions is proposed.

In the framework of LES of turbulent flows, the deconvolved integral NS equations can be interpreted as the governing equations for the explicit-filtering LES, corresponding to the application of a high-order filter. In fact, the deconvolution of the volume-averaged solution, along with the high-order flux reconstruction, is performed at every time step. Hence, one really solves the evolution equation for the approximately deconvolved variable, that resembles that one reported in Reference [31]. In this respect, the present method is naturally related to other approximate deconvolution-based procedures which, however, were developed for modelling the evolution equations for the volume-averaged solution [32–35]. Actually, these models, which were originally applied for LES based upon the differential form of the governing equations, are here extended to the FV integral formulation, leading to some significant modifications.

Some numerical results are obtained, for both the simply averaged velocity and the deconvolved one, by supplying the LES equations with mixed models (i.e. scale-similarity model plus eddy-viscosity one). Some insights into the performances of different FV based LES formulations are provided.

Finally, the outline of the paper is as follows: After introducing the governing equations for the deconvolved field in the next section, the entire numerical procedure is detailed in Section 3, where the specific feature of the consistent discretization of the inverse deconvolution operator is also discussed. Section 4 is devoted to the clarification of how the present formulation can be interpreted in the framework of LES of incompressible flows. Numerical results for both an exact unsteady NS solution and a real flow prototype, i.e. the time evolving mixing layer, are presented in Section 5. These results clearly demonstrate the validity of the proposed method and the advantages of having a fourth-order accurate velocity field, as traced in the concluding section.

2. DECONVOLVED INTEGRAL NAVIER–STOKES EQUATIONS ON NON-UNIFORM GRIDS

Consider, in a bounded computational domain V, the flow of an incompressible fluid with constant properties. The integral non-dimensional NS equations are written over a FV $\Omega(\mathbf{x}) \subseteq V$, centred in $\mathbf{x}$, as

$$\int_{\partial\Omega(\mathbf{x})} \mathbf{v} \cdot \mathbf{n} \, \mathrm{d}S = 0 \tag{1}$$

$$\frac{\partial \bar{\mathbf{v}}}{\partial t} = -\frac{1}{|\Omega(\mathbf{x})|} \int_{\partial\Omega(\mathbf{x})} \mathbf{F} \cdot \mathbf{n} \, \mathrm{d}S \tag{2}$$

where $|\Omega(\mathbf{x})|$ is the FV measure and $\mathbf{n}$ the local unit vector outward the boundary $\partial\Omega(\mathbf{x})$. Moreover, $\mathbf{F}(\mathbf{v}) = \mathbf{v}\mathbf{v} + \mathbf{I}p - (1/Re)(\underline{\nabla}\mathbf{v} + \underline{\nabla}^{\mathrm{T}}\mathbf{v})$ stands for the momentum flux tensor, $\mathbf{v}$ being the velocity vector, $\mathbf{I}p$ the pressure stress tensor and Re the Reynolds number. Proper boundary conditions on ∂V must be prescribed in order to integrate the system (1)–(2), starting from a divergence-free initial velocity. In Equation (2), the local volume-averaged velocity $\bar{\mathbf{v}}$ is

defined according to:

$$\bar{\mathbf{v}}(\mathbf{x},t)=\frac{1}{|\Omega(\mathbf{x})|}\int_{\Omega(\mathbf{x})}\mathbf{v}(\mathbf{x}',t)\,\mathrm{d}\mathbf{x}' \tag{3}$$

Following the formulation proposed in References [17–19], by performing a mth order Taylor-series expansion of $\mathbf{v}$ around the FV centre $\mathbf{x}$, Equation (3) can be rewritten as

$$\bar{\mathbf{v}}(\mathbf{x})=(I_{\mathbf{x}}-R_{\mathbf{x}}^{(m)})\mathbf{v}+\cdots \tag{4}$$

where, for sake of brevity, time dependence was omitted. In the previous relation, $I_{\mathbf{x}}\mathbf{v}=\mathbf{v}(\mathbf{x})$ and the mth order differential operator

$$R_{\mathbf{x}}^{(m)}\equiv-\sum_{l=1}^{m}\frac{1}{l!}\sum_{l_1+l_2+l_3=l}C_{l_1,l_2,l_3}(\mathbf{x})D_{\mathbf{x}}^{(l_1,l_2,l_3)}$$

was introduced, $D_{\mathbf{x}}^{(l_1,l_2,l_3)}=\partial_{x_1}^{l_1}\partial_{x_2}^{l_2}\partial_{x_3}^{l_3}$ being the lth order three-dimensional derivative in a Cartesian reference system and

$$C_{l_1,l_2,l_3}(\mathbf{x})=\frac{1}{|\Omega(\mathbf{x})|}\prod_{k=1}^{3}\int_{\Omega(\mathbf{x})}(x_k'-x_k)^{l_k}\,\mathrm{d}\mathbf{x}'$$

standing for the coefficients in the sum. Note that, for non-uniform grids, these coefficients effectively are space dependent. Starting from (4), the unfiltered velocity can be approximately expressed in terms of the filtered one as

$$\mathbf{v}(\mathbf{x})=(I_{\mathbf{x}}+R_{\mathbf{x}}^{(m)}+[R_{\mathbf{x}}^{(m)}]^{(2)}+\cdots)\bar{\mathbf{v}}$$

Thus, a higher-order filtered velocity is defined by truncating the previous expansion according to

$$\tilde{\mathbf{v}}(\mathbf{x})\equiv A_{\mathbf{x}}^{(m)}\bar{\mathbf{v}} \tag{5}$$

$A_{\mathbf{x}}^{(m)}$ standing for the mth order truncated deconvolution differential operator. Let us note that the adoption of truncated series expansion is a well-known procedure in regularizing ill-posed problems (e.g. [31, 34, 35]). This way, since $\mathbf{v}(\mathbf{x})=\tilde{\mathbf{v}}(\mathbf{x})+O(h^{m+1})$, h being the linear extension of the FV (e.g. $h=|\Omega(\mathbf{x})|^{1/3}$), the deconvolved velocity field $\tilde{\mathbf{v}}$ represents an mth order approximant to $\mathbf{v}$. Henceforth, as a consequence of definition (5), Equation (2) can be rewritten as a balance equation for $\tilde{\mathbf{v}}$, that is

$$\frac{\partial\tilde{\mathbf{v}}}{\partial t}=-A_{\mathbf{x}}^{(m)}\left[\frac{1}{|\Omega|}\int_{\partial\Omega}\mathbf{F}\cdot\mathbf{n}\,\mathrm{d}S\right] \tag{6}$$

Observe that, as usual in FV procedures, Equation (6) needs closure modelling since the flux $\mathbf{F}$ depends onto the unfiltered velocity $\mathbf{v}$. Moreover, owing to the lack of commutativity between deconvolution and integration, a commutation vector term, say $\mathbf{m}$, should be considered such that

$$\frac{\partial\tilde{\mathbf{v}}}{\partial t}=\mathbf{m}-\frac{1}{|\Omega|}\int_{\partial\Omega}A_{\mathbf{x}'}^{(m)}\mathbf{F}\cdot\mathbf{n}\,\mathrm{d}S \tag{7}$$

Actually, for uniform grids, $\mathbf{m}$ identically vanishes and (7) becomes a conservation equation for $\tilde{\mathbf{v}}$. Here, the proposed formulation holds a suitable strategy to avoid the explicit computation of $\mathbf{m}$ for non-uniform grids. This is accomplished by resolving the following modified momentum equation:

$$[A_{\mathbf{x}}^{(m)}]^{-1}\frac{\partial\tilde{\mathbf{v}}}{\partial t}=-\frac{1}{|\Omega(\mathbf{x})|}\int_{\partial\Omega(\mathbf{x})}\mathbf{F}\cdot\mathbf{n}\,\mathrm{d}S \tag{8}$$

in which the inverse of the deconvolution operator has been directly applied onto the velocity time derivative. Also in this form, Equation (8) still stands for the evolution equation for the high-order filtered velocity $\tilde{\mathbf{v}}$. Alternatively, one could evaluate the RHS of Equation (8), solve for $\bar{\mathbf{v}}$ and then explicitly perform the deconvolution at each time step. The present procedure is not the same as solving Equation (2) for $\bar{\mathbf{v}}$ and then obtaining $\tilde{\mathbf{v}}$, during a post-processing step, after the computation of the flow field is finished, as proposed in Reference [16]. In order to point out the implicit character of the proposed formulation, the notation $[A_{\mathbf{x}}^{(m)}]^{-1}$ is left in the following.

As regards the continuity constraint, Equation (1) must be rewritten in terms of the resolved velocity field as $\int_{\partial\Omega(\mathbf{x})}\mathbf{n}\cdot\mathbf{v}\,\mathrm{d}S=q+\int_{\partial\Omega(\mathbf{x})}\mathbf{n}\cdot\tilde{\mathbf{v}}\,\mathrm{d}S=0$, where q stands again for the commutation error term arising for non-uniform grids.

Since both the momentum and the continuity equations are not in a closed form, suitable closure relations must be supplied. However, when the FV grid is sufficiently fine, the approximation $\mathbf{F}(\mathbf{v})\cong\mathbf{F}(\tilde{\mathbf{v}})$ can be considered in Equation (8) and, congruently, $q=0$ can be assumed in the continuity equation. Thus, by fixing $m=2$ denoting $A_{\mathbf{x}}^{(2)}=A$, the deconvolved integral NS equations are rewritten as

$$\begin{gathered}\int_{\partial\Omega(\mathbf{x})}\mathbf{v}\cdot\mathbf{n}\,\mathrm{d}S=0\\ A^{-1}\frac{\partial\mathbf{v}}{\partial t}=\mathbf{I}_{\mathrm{conv}}+\mathbf{I}_{\mathrm{diff}}+\mathbf{I}_{\mathrm{press}}\end{gathered} \tag{9}$$

having defined the vector fields

$$\begin{aligned}\mathbf{I}_{\mathrm{conv}}&=-\frac{1}{|\Omega(\mathbf{x})|}\int_{\partial\Omega(\mathbf{x})}\mathbf{v}\mathbf{v}\cdot\mathbf{n}\,\mathrm{d}S\\ \mathbf{I}_{\mathrm{press}}&=-\frac{1}{|\Omega(\mathbf{x})|}\int_{\partial\Omega(\mathbf{x})}p\mathbf{n}\,\mathrm{d}S\\ \mathbf{I}_{\mathrm{diff}}&=\frac{1}{Re|\Omega(\mathbf{x})|}\int_{\partial\Omega(\mathbf{x})}(\underline{\nabla}\mathbf{v}+\underline{\nabla}^{\mathrm{T}}\mathbf{v})\cdot\mathbf{n}\,\mathrm{d}S\equiv\frac{1}{Re}D\mathbf{v}\end{aligned} \tag{10}$$

along with the integro-differential operator

$$D(\,)\equiv\frac{1}{|\Omega(\mathbf{x})|}\int_{\partial\Omega(\mathbf{x})}[\underline{\nabla}(\,)+\underline{\nabla}^{\mathrm{T}}(\,)]\cdot\mathbf{n}\,\mathrm{d}S \tag{11}$$

The numerical procedure adopted for solving the governing equations (9) is discussed in detail in the next section.

In a different manner, for coarse FV grids, Equation (8) must be interpreted as a LES equation for the high-order filtered velocity $\tilde{\mathbf{v}}$, to be supplied with some suitable SGS modelling, as discussed in Section 4.

3. THE NUMERICAL PROCEDURE

In this section, the numerical procedure for the time-dependent solution of the deconvolved integral NS equations (9) is introduced and a fourth-order accurate FV discretization is presented. For the sake of simplicity, the numerical method is illustrated in two spatial dimensions. A computational domain $V = [0, L_1] \times [0, L_2]$ is assumed, (x, y) standing for the spatial co-ordinates and (u, v) for the velocity components. The time integration is performed by means of a semi-implicit second-order accurate scheme, while the velocity–pressure decoupling is obtained by means of the *pressure-free* FTS method (e.g. References [24–26]). As regards the spatial discretization, a co-located grid arrangement of the variables was preferred because of its computational simplicity. This choice implies that the fluxes, defined along the FV boundary, must be approximated in terms of the balanced variables, located at the FV centre. In the following sub-sections, the adopted grid definition, the time integration and the space discretization are detailed. Furthermore, the consistent discretization of the inverse deconvolution operator is illustrated and the issue of the high-order boundary conditions assignment for the FTS method is discussed.

3.1. Two-dimensional grid definition

The domain V is partitioned by means of a two-dimensional (2-D) Cartesian non-uniform structured grid, as sketched in Figure 1. Along the x-direction, assumed to be homogeneous,

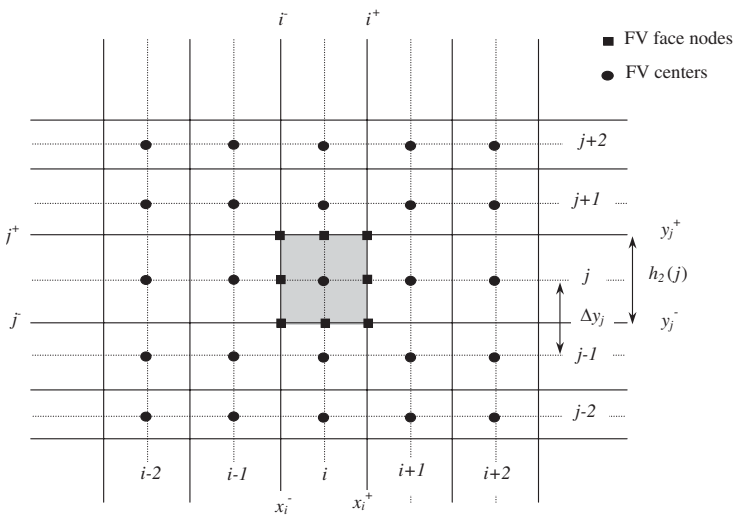

Figure 1. Sketch of the adopted 2-D computational FV grid, non-uniform in the y-direction; (x_i, y_j) stands for the FV centre node.

the FV centres are uniformly distributed, i.e. $x_i = (i - \frac{1}{2})h_1,\ (i = 1, \ldots, N_1),\ h_1 = L_1/N_1$ being the step size and N_1 the number of FVs in this direction. Along the y-direction, assumed to be normal to a wall, a non-uniform grid is introduced by means of a 1-D mapping $y = Y(\zeta),\ \zeta$ being the independent variable in the transformed domain. The latter is uniformly partitioned according to $\zeta_k = (k-1)H,\ (k = 1, \ldots, N_2 + 1),\ H = L_2/N_2$ being the grid-spacing and N_2 the number of FVs in y-direction. Thus, the FV face co-ordinates in the physical space are defined by $y_j^- = Y(\zeta_j)$ and $y_j^+ = Y(\zeta_{j+1}),\ (j = 1, \ldots, N_2)$ and the FV centre is located at

$$y_j = (y_j^- + y_j^+)/2$$

Moreover, the distance between two adjacent FV centres is defined as

$$\Delta y_j \equiv y_j - y_{j-1} = \frac{(y_j^+ - y_{j-1}^-)}{2}, \quad (j = 2, \ldots, N_2)$$

while the FV width along the y-direction is

$$h_2(j) = y_j^+ - y_j^- = Y(\zeta_{j+1}) - Y(\zeta_j) = HY'(\zeta_j) + H^2 Y''(\zeta_j)/2 + \cdots$$

Let us note that a smooth mapping is assumed, so that $h_2/H = O(1)$. Finally, one has the FV definition $\Omega(x_i, y_j) \equiv \Omega_{ij} = [x_i^-, x_i^+] \times [y_j^-, y_j^+]$, where the face co-ordinates can be expressed in terms of the cell centre co-ordinates as

$$x_i^- = x_i - h_1/2, \quad x_i^+ = x_i + h_1/2$$

$$y_j^- = y_j - h_2(j)/2, \quad y_j^+ = y_j + h_2(j)/2$$

Henceforth, the explicit dependence of h_2 from j is omitted and $Y'(\zeta_j)$ is denoted as Y_j'.

3.2. Time integration and pressure–velocity decoupling

The time integration of the momentum equation $(9)_2$ is based on the classical second-order semi-implicit AB/CN scheme. In particular, the diffusive terms along the y-axis are integrated according to the CN approximation, while the AB time-extrapolation is adopted for all the others. According to such integration method, the corresponding discretized momentum equation, along with the associated Dirichlet boundary conditions, becomes:

$$\begin{aligned} \left(A^{-1} - \frac{\Delta t}{2Re} D_2\right)\mathbf{v}^{n+1} = \left(A^{-1} + \frac{\Delta t}{2Re} D_2\right)\mathbf{v}^n + \frac{\Delta t}{2}\left[3\left(\frac{1}{Re} D_1 \mathbf{v}^n + \mathbf{I}_{\text{conv}}^n\right)\right. \\ \left. - \left(\frac{1}{Re} D_1 \mathbf{v}^{n-1} + \mathbf{I}_{\text{conv}}^{n-1}\right)\right] + \int_{t^n}^{t^{n+1}} \mathbf{I}_{\text{press}}\, \mathrm{d}t \\ \mathbf{v}^{n+1} = \mathbf{v}_b^{n+1} \quad \text{on } \partial V \end{aligned} \tag{12}$$

In reality, one should consider boundary conditions for the actual high-order averaged velocity but, as usual, the physical conditions are directly exploited. Note how, in Equation (12),

the operator (11) was split along the Cartesian directions as $D = D_1 + D_2$, with

$$\begin{aligned} D_1(\,) &\equiv \frac{1}{|\Omega(\mathbf{x})|}\int_{y^-}^{y^+}\left(\frac{\partial}{\partial\xi}\bigg|_{x^+} - \frac{\partial}{\partial\xi}\bigg|_{x^-}\right)\mathrm{d}\eta \\ D_2(\,) &\equiv \frac{1}{|\Omega(\mathbf{x})|}\int_{x^-}^{x^+}\left(\frac{\partial}{\partial\eta}\bigg|_{y^+} - \frac{\partial}{\partial\eta}\bigg|_{y^-}\right)\mathrm{d}\xi \end{aligned} \tag{13}$$

$x^{\pm}$ and $y^{\pm}$ being the FV face co-ordinates.

The velocity–pressure de-coupling is obtained by means of the *pressure-free* FTS method, which is based on a prediction step, where a non-solenoidal vector field $\mathbf{v}^*$ is obtained by solving Equation (12) without considering the pressure term, along with proper intermediate boundary conditions:

$$\begin{aligned} \left(A^{-1} - \frac{\Delta t}{2Re}D_2\right)\mathbf{v}^* &= \left(A^{-1} + \frac{\Delta t}{2Re}D_2\right)\mathbf{v}^n \\ &\quad + \frac{\Delta t}{2}\left[3\left(\frac{1}{Re}D_1\mathbf{v}^n + \mathbf{I}^n_{\mathrm{conv}}\right) - \left(\frac{1}{Re}D_1\mathbf{v}^{n-1} + \mathbf{I}^{n-1}_{\mathrm{conv}}\right)\right] \\ \mathbf{v}^* &= \mathbf{v}^*_b \quad \text{on } \partial V \end{aligned} \tag{14}$$

Then, in order to obtain a divergence-free vector field, the intermediate velocity is corrected in the projection step. That is, according to the Helmholtz–Hodge decomposition, $\mathbf{v}^*$ is expressed as the sum of the unknown divergence-free velocity $\mathbf{v}^{n+1}$ and a pure gradient field

$$\mathbf{v}^{n+1} = \mathbf{v}^* - \underline{\nabla}\phi \tag{15}$$

By imposing the continuity constraint $(9)_1$ the unknown field ϕ must satisfy the equation:

$$(D_1 + D_2)\phi = \frac{1}{|\Omega(\mathbf{x})|}\int_{\partial\Omega(\mathbf{x})}\mathbf{n}\cdot\mathbf{v}^*\,\mathrm{d}S \tag{16}$$

associated with proper normal boundary conditions

$$\frac{\partial\phi}{\partial n} = \mathbf{n}\cdot(\mathbf{v}^*_b - \mathbf{v}^{n+1}_b) \quad \text{on } \partial V \tag{17}$$

It is noteworthy that the use of the CN scheme, though relaxing the stability constraints, nevertheless introduces a first-order approximation in the evaluation of the actual pressure field. In fact, by substituting Equation (15) into $(12)_1$ and exploiting (14), remembering the definitions (3) and $(10)_2$, one gets the relation between the gradient term and the actual pressure gradient field:

$$\int_{t^n}^{t^{n+1}}\overline{\underline{\nabla}p}\,\mathrm{d}t = \left(A^{-1} - \frac{\Delta t}{2Re}D_2\right)\underline{\nabla}\phi \tag{18}$$

that, owing to (13), becomes

$$\overline{\int_{t^n}^{t^{n+1}}\underline{\nabla}p\,\mathrm{d}t} = \left(A^{-1}\underline{\nabla}\phi - \frac{\Delta t}{2Re}\overline{\frac{\partial^2\underline{\nabla}\phi}{\partial y^2}}\right) = \overline{\left(I - \frac{\Delta t}{2Re}\frac{\partial^2}{\partial y^2}\right)\underline{\nabla}\phi} \tag{19}$$

whereby the last equality holds to fourth-order accuracy. Finally, since this relation holds for any FV size, one obtains

$$\underline{\nabla}\int_{t^n}^{t^{n+1}} p\,\mathrm{d}t = \left(I - \frac{\Delta t}{2Re}\,\frac{\partial^2}{\partial y^2}\right)\underline{\nabla}\phi \tag{20}$$

from which it is evident that $\underline{\nabla}\phi$ approximates the actual time integrated pressure gradient only to first-order time accuracy. When required, for example for post-processing purposes, the pressure field can be better evaluated by fully exploiting the above relation (e.g. Reference [26]).

Finally, in order to retain a real second-order time-accurate solution, proper boundary conditions for computing the intermediate velocity field are required. This issue will be described in Section 3.4, for both the prediction and the projection steps.

3.3. Fourth-order spatial discretization

This section illustrates the technique adopted for performing the spatial discretization of Equations (14) and (16) over a general FV, say $\Omega_{i,j}$. The line integration along the FV faces is performed by means of the Simpson rule, while the Lagrangian interpolation is exploited for flux reconstruction. Even though, for a given accuracy order, the Lagrangian interpolation involves a wider stencil than the Hermitian one (adopted, for example, in Reference [16]), the former remains simply applicable also on non-uniform meshes. Finally, it will be shown that the discretization of the approximate inverse deconvolution operator does not further enlarge the stencil already involved by the flux integration.

3.3.1. Line integrals discretization. The line integrals in Equations (14) and (16) are discretized to fourth-order accuracy by means of the Simpson formula applied in each direction. For a generic function f, one has:

$$\frac{1}{h_2}\int_{y_j^-}^{y_j^+} f(x_i^{\pm},\eta)\,\mathrm{d}\eta = \frac{1}{6}(f_{i^{\pm},j^+} + 4f_{i^{\pm},j} + f_{i^{\pm},j^-}) - \frac{h_2^4}{2880}\left.\frac{\partial^4 f}{\partial y^4}\right|_{i^{\pm},j} + \cdots \tag{21}$$

wherein $f_{i^{\pm},j^{\pm}} \equiv f(x_i^{\pm}, y_j^{\pm})$. Thus, when considering the net flux along the x-axis one has:

$$\frac{1}{h_1 h_2}\int_{y_j^-}^{y_j^+} [f(x_i^+,\eta) - f(x_i^-,\eta)]\,\mathrm{d}\eta = \frac{1}{6h_1}(f_{i,j^+} + 4f_{i,j} + f_{i,j^-})\Big|_{i^-}^{i^+} - \frac{h_2^4}{2880}\left.\frac{\partial^5 f}{\partial x \partial y^4}\right|_{i,j} + \cdots \tag{22}$$

and, analogously, for the net flux along the y-axis,

$$\frac{1}{h_1 h_2}\int_{x_i^-}^{x_i^+} [f(\xi,y_j^+) - f(\xi,y_j^-)]\,\mathrm{d}\xi = \frac{1}{6h_2}(f_{i^+,j} + 4f_{i,j} + f_{i^-,j})\Big|_{j^-}^{j^+} - \frac{h_1^4}{2880}\left.\frac{\partial^5 f}{\partial x^4 \partial y}\right|_{i,j} + \cdots \tag{23}$$

During the interpolation procedure, illustrated in the next sub-section, the function f in Equations (22,23) represent a component of either the convective flux tensor $\mathbf{vv}$, or the diffusive one $(\underline{\nabla}\mathbf{v} + \underline{\nabla}^{\mathrm{T}}\mathbf{v})/Re$.

3.3.2. Flux interpolation procedure. Similarly to the procedure adopted in Reference [15], in Equations (22) and (23) the face-node unknowns are expressed in terms of the FV centre values by performing cubic Lagrangian interpolations. The consequent discretization of the terms $\mathbf{I}_{\mathrm{conv}}$ and $\mathbf{I}_{\mathrm{diff}}$, defined in (10), is illustrated.

When f stands for an advective flux component (i.e. one among u^2, v^2, uv), by exploiting 1-D interpolations along the grid line in x-direction, the mid-point values $f_{i^{\pm},j}$, are approximated by $\hat{f}_{i^{\pm},j}$ according to

$$\hat{f}_{i^{\pm},j} = \frac{1}{16}(9f_{i\pm1,j} + 9f_{i,j} - f_{i\mp1,j} - f_{i\pm2,j}) \tag{24}$$

while, in the other direction, for example at the mid-section point j^{+}, one has

$$\hat{f}_{i,j^{+}} = \frac{1}{8}\sum_{p=-1}^{2} a_p f_{i,j+p} \tag{25}$$

where the coefficients a_p, reported in Table I, depend on the position along the non-uniform direction. A similar formula for $\hat{f}_{i,j^{-}}$ is obtained by simply shifting the index, being not reported for the sake of brevity. It can be shown that the interpolation error corresponding to the approximation (24) is

$$f_{i^{\pm},j} - \hat{f}_{i^{\pm},j} = \frac{3}{128}h_1^4 \left.\frac{\partial^4 f}{\partial x^4}\right|_{i^{\pm},j} + \cdots \tag{26}$$

having exploited a Taylor-series expansion of the grid mapping law about y_j. As regards with the four corner values, they require successive applications of interpolations (24) and (25). For example, the value $f_{i^{+},j^{+}}$ is approximated by first applying the relation (24) at $(i^{+}, j+p)$ with $p=-1,\ldots,2$; then, according to Equation (25), the interpolation along the y-direction provides

$$\begin{aligned}\hat{f}_{i^{+},j^{+}} &= \frac{1}{8}\sum_{p=-1}^{2} a_p \hat{f}_{i^{+},j+p} \\ &= \frac{1}{128}\sum_{p=-1}^{2} a_p[9(f_{i+1,j+p} + f_{i,j+p}) - (f_{i-1,j+p} + f_{i+2,j+p})]\end{aligned} \tag{27}$$

which globally involves sixteen FV centres. Similarly, one proceeds to approximating the other corner values and the corresponding interpolation errors are

$$f_{i^{\pm},j^{\pm}} - \hat{f}_{i^{\pm},j^{\pm}} = \frac{3}{128}h_1^4 \left.\frac{\partial^4 f}{\partial x^4}\right|_{i^{\pm},j^{\pm}} + \frac{3}{128}H^4(Y_j')^4 \left.\frac{\partial^4 f}{\partial y^4}\right|_{i^{\pm},j^{\pm}} + \cdots \tag{28}$$

Table I. Interpolation coefficients a_p in Equation (25) and b_p in Equation (32), for a given position j along the non-homogeneous direction; it is assumed $h_2 = h_2(j)$.

p	a_p	b_p
-1	$\dfrac{-h_2(h_2 - 2\Delta y_{j+1})(h_2 - 2\Delta y_{j+2} - 2\Delta y_{j+1})}{\Delta y_j(\Delta y_{j+1} + \Delta y_j)(\Delta y_{j+2} + \Delta y_{j+1} + \Delta y_j)}$	$\dfrac{\frac{-3}{4}h_2^2 + h_2(\Delta y_{j+2} + 2\Delta y_{j+1}) - \Delta y_{j+1}(\Delta y_{j+2} + \Delta y_{j+1})}{\Delta y_j(\Delta y_{j+1} + \Delta y_j)(\Delta y_{j+2} + \Delta y_{j+1} + \Delta y_j)}$
0	$\dfrac{-(h_2 - 2\Delta y_{j+1})(h_2 + 2\Delta y_j)(h_2 - 2(\Delta y_{j+1} + \Delta y_{j+2}))}{\Delta y_j\Delta y_{j+1}(\Delta y_{j+2} + \Delta y_{j+1})}$	$\dfrac{\frac{3}{4}h_2^2 + h_2(\Delta y_j - 2\Delta y_{j+1}) - \Delta y_{j+1}\Delta y_j - (\Delta y_j - \Delta y_{j+1})(\Delta y_{j+1} + \Delta y_{j+2})}{\Delta y_j\Delta y_{j+1}(\Delta y_{j+2} + \Delta y_{j+1})}$
1	$\dfrac{-h_2(h_2 + 2\Delta y_j)(h_2 - 2\Delta y_{j+1} - 2\Delta y_{j+2})}{\Delta y_{j+1}\Delta y_{j+2}(\Delta y_j + \Delta y_{j+1})}$	$\dfrac{-\frac{3}{4}h_2^2(j) - h_2(j)(\Delta y_j - \Delta y_{j+1} - \Delta y_{j+1}) + \Delta y_j(\Delta y_{j+1} + \Delta y_{j+2})}{\Delta y_{j+1}\Delta y_{j+1}(\Delta y_j + \Delta y_{j+1})}$
2	$\dfrac{-h_2(h_2 - 2\Delta y_{j+1})(h_2 - 2\Delta y_j)}{\Delta y_{j+2}(\Delta y_{j+1} + \Delta y_{j+2})(\Delta y_{j+2} + \Delta y_{j+1} + \Delta y_j)}$	$\dfrac{\frac{3}{4}h_2^2(j) + h_2(j)(\Delta y_j - \Delta y_{j+1}) - \Delta y_j\Delta y_{j+1}}{\Delta y_{j+2}(\Delta y_{j+1} + \Delta y_{j+2})(\Delta y_{j+2} + \Delta y_{j+1} + \Delta y_j)}$

Concerning the discretization of $\mathbf{I}_{\text{conv}}$, one can rewrite (22) as

$$\frac{1}{h_1 h_2}\int_{y_j^-}^{y_j^+}[f(x_i^+,\eta)-f(x_i^-,\eta)]\,\mathrm{d}\eta = \frac{1}{6h_1}(\hat{f}_{i,j^+}+4\hat{f}_{i,j}+\hat{f}_{i,j^-})\Big|_{i^-}^{i^+} + \frac{3}{128}\frac{h_1^4 HY_j'}{h_2}\left.\frac{\partial^5 f}{\partial x^5}\right|_{i,j} + \frac{1}{128}\frac{(HY_j')^5}{h_2}\left.\frac{\partial^5 f}{\partial x\partial y^4}\right|_{i,j} - \frac{h_2^4}{2880}\left.\frac{\partial^5 f}{\partial x\partial y^4}\right|_{i,j}+\cdots \tag{29}$$

and (23) as

$$\frac{1}{h_1 h_2}\int_{x_i^-}^{x_i^+}[f(\xi,y_j^+)-f(\xi,y_j^-)]\,\mathrm{d}\xi = \frac{1}{6h_2}(\hat{f}_{i^+,j}+4\hat{f}_{i,j}+\hat{f}_{i^-,j})\Big|_{j^-}^{j^+} + \frac{h_1^4}{128}\frac{HY_j'}{h_2}\left.\frac{\partial^5 f}{\partial x^4\partial y}\right|_{i,j} + \frac{3}{128}\frac{(HY_j')^5}{h_2}\left.\frac{\partial^5 f}{\partial y^5}\right|_{i,j} - \frac{h_1^4}{2880}\left.\frac{\partial^5 f}{\partial x^4\partial y}\right|_{i,j}+\cdots \tag{30}$$

These equations show a fourth-order leading truncation error since, for vanishing grid spacing, HY_j'/h_2 tends toward unity.

On the other hand, when f stands for a diffusive flux component, that is $\partial g/\partial x$ or $\partial g/\partial y$, g standing for a velocity vector component, the mid-point values $(\partial g/\partial x)_{i^\pm,j}$ are approximated by

$$\left(\widehat{\frac{\partial g}{\partial x}}\right)_{i^\pm,j} = \pm\frac{1}{24h_1}(27g_{i\pm1,j}-27g_{i,j}+g_{i\mp1,j}-g_{i\pm2,j}) \tag{31}$$

while in the non-uniform direction, for example at the mid-section point j^+, the value $(\partial g/\partial y)_{i,j^+}$ is given by

$$\left(\widehat{\frac{\partial g}{\partial y}}\right)_{i,j^+} = \sum_{p=-1}^{2} b_p g_{i,j+p} \tag{32}$$

the coefficients b_p being reported in Table I. By shifting the index j, a similar expression for the value $(\widehat{\partial g/\partial y})_{i,j^-}$ is obtained. It is noteworthy remarking that Equations (31) and (32) were obtained first by approximating g with a cubic polynomial and then differentiating it.

The errors corresponding to the above approximations are

$$\left(\frac{\partial g}{\partial x}\right)_{i^{\pm},j} - \left(\widehat{\frac{\partial g}{\partial x}}\right)_{i^{\pm},j} = \frac{3h_1^4}{640}\left.\frac{\partial^5 g}{\partial x^5}\right|_{i^{\pm},j} + \cdots$$
$$\left(\frac{\partial g}{\partial y}\right)_{i,j^{\pm}} - \left(\widehat{\frac{\partial g}{\partial y}}\right)_{i,j^{\pm}} = (HY_j')^4\left[\frac{3}{640}\left.\frac{\partial^5 g}{\partial y^5}\right|_{i,j^{\pm}} + \frac{7}{96}\frac{Y_j''}{(Y_j')^2}\left.\frac{\partial^4 g}{\partial y^4}\right|_{i,j^{\pm}}\right] + \cdots \tag{33}$$

respectively.

As regards the evaluation of diffusive fluxes at a corner node, both x and y derivatives are required in Equations (22,23). Therefore, a strategy similar to that adopted for obtaining Equation (27) is exploited. For example, in order to approximate $(\partial g/\partial x)_{i^+,j^+}$, one first applies the approximate derivative (31) at $(i^+, j+p)$ with $p=-1,\ldots,2$; then, according to Equation (25), the interpolation along the y-direction provides

$$\left(\widehat{\frac{\partial g}{\partial x}}\right)_{i^+,j^+} = \frac{1}{8}\sum_{p=-1}^{2} a_p \left(\widehat{\frac{\partial g}{\partial x}}\right)_{i^+,j+p}$$
$$= \frac{1}{192h_1}\sum_{p=-1}^{2} a_p(27g_{i+1,j+p} - 27g_{i,j+p} + g_{i-1,j+p} - g_{i+2,j+p}) \tag{34}$$

In a similar manner, one proceeds in approximating $(\partial g/\partial y)_{i^+,j^+}$, that is, one first applies the approximate derivative (32) at $(i+p, j^+)$ with $p=-1,\ldots,2$; then, according to Equation (24), the interpolation along the x-direction provides

$$\left(\widehat{\frac{\partial g}{\partial y}}\right)_{i^+,j^+} = \frac{1}{16}\left[9\left(\widehat{\frac{\partial g}{\partial y}}\right)_{i+1,j} + 9\left(\widehat{\frac{\partial g}{\partial y}}\right)_{i,j} - \left(\widehat{\frac{\partial g}{\partial y}}\right)_{i-1,j} - \left(\widehat{\frac{\partial g}{\partial y}}\right)_{i+2,j}\right]$$
$$= \frac{1}{16}\sum_{p=-1}^{2} b_p[9(g_{i+1,j+p} + g_{i,j+p}) - (g_{i-1,j+p} + g_{i+2,j+p})] \tag{35}$$

By shifting the index j, one can obtain the approximations for the other three corner nodes. The corresponding interpolation errors associated with expressions (34) and (35), are

$$\left(\frac{\partial g}{\partial x}\right)_{i^+,j^+} - \left(\widehat{\frac{\partial g}{\partial x}}\right)_{i^+,j^+} = \frac{3h_1^4}{640}\left.\frac{\partial^5 g}{\partial x^5}\right|_{i^+,j^+} + \frac{3(h_1 Y_j')^4}{128}\left.\frac{\partial^5 g}{\partial y^4 \partial x}\right|_{i^+,j^+} + \cdots$$
$$\left(\frac{\partial g}{\partial y}\right)_{i^+,j^+} - \left(\widehat{\frac{\partial g}{\partial y}}\right)_{i^+,j^+} = \frac{3h_1^4}{128}\left.\frac{\partial^5 g}{\partial x^4 \partial y}\right|_{i^+,j^+} + (HY_j')^4\left[\frac{3}{640}\left.\frac{\partial^5 g}{\partial y^5}\right|_{i^+,j^+}\right.$$
$$\left. + \frac{7}{96}\frac{Y_j''}{(Y_j')^2}\left.\frac{\partial^4 g}{\partial y^4}\right|_{i^+,j^+}\right] + \cdots \tag{36}$$

respectively.

Finally, as far as the discretization of $\mathbf{I}_{\text{diff}}$ is concerned, Equation (22) rewrites as

$$
\begin{aligned}
D_1|_{i,j}g &\equiv \frac{1}{h_1 h_2}\int_{y_j^-}^{y_j^+}\left(\left.\frac{\partial g}{\partial \xi}\right|_{x_i^+} - \left.\frac{\partial g}{\partial \xi}\right|_{x_i^-}\right)\mathrm{d}\eta \\
&= \frac{1}{6h_1}\left[\left(\widehat{\frac{\partial g}{\partial x}}\right)_{i,j^+} + 4\left(\widehat{\frac{\partial g}{\partial x}}\right)_{i,j} + \left(\widehat{\frac{\partial g}{\partial x}}\right)_{i,j^-}\right]\Bigg|_{i^-}^{i^+} \\
&\quad + \frac{3}{640}\frac{h_1^4 H Y_j'}{h_2}\left.\frac{\partial^6 g}{\partial x^6}\right|_{i,j} + \frac{1}{128}\frac{(HY_j')^5}{h_2}\left.\frac{\partial^6 g}{\partial x^2 \partial y^4}\right|_{i,j} - \frac{h_2^4}{2880}\left.\frac{\partial^6 g}{\partial x^2 \partial y^4}\right|_{i,j} + \cdots
\end{aligned}
\tag{37}
$$

and (23) as

$$
\begin{aligned}
D_2|_{i,j}g &\equiv \frac{1}{h_1 h_2}\int_{x_i^-}^{x_i^+}\left(\left.\frac{\partial g}{\partial \eta}\right|_{y_j^+} - \left.\frac{\partial g}{\partial \eta}\right|_{y_j^-}\right)\mathrm{d}\xi \\
&= \frac{1}{6h_2}\left[\left(\widehat{\frac{\partial g}{\partial y}}\right)_{i^+,j} + 4\left(\widehat{\frac{\partial g}{\partial y}}\right)_{i,j} + \left(\widehat{\frac{\partial g}{\partial y}}\right)_{i^-,j}\right]\Bigg|_{j^-}^{j^+} + \frac{7}{96}\frac{(HY_j')^5}{h_2}\frac{Y_j''}{(Y_j')^2}\left.\frac{\partial^5 g}{\partial y^5}\right|_{i,j} \\
&\quad + \frac{3}{640}\frac{(HY_j')^5}{h_2}\left.\frac{\partial^6 g}{\partial y^6}\right|_{i,j} + \frac{1}{128}\frac{h_1^4 H Y_j'}{h_2}\left.\frac{\partial^6 g}{\partial x^4 \partial y^2}\right|_{i,j} - \frac{h_1^4}{2880}\left.\frac{\partial^6 g}{\partial x^4 \partial y^2}\right|_{i,j} + \cdots
\end{aligned}
\tag{38}
$$

These relations are also exploited for discretizing the LHS of the projection equation (16), the RHS being approximated according to the procedure adopted for $\mathbf{I}_{\text{conv}}$. According to the proposed discretization, a twenty-five grid-nodes computational molecule for both the prediction and the projection steps is obtained. The strong even–odd coupling, associated with such stencil, guarantees that no spurious solutions are produced.

3.3.3. High-order discrete deconvolution. For a symmetric cell construction, the approximate inverse deconvolution operation appearing in Equation (9), rewrites as

$$
A^{-1}\tilde{\mathbf{v}} \equiv \left(I_{\mathbf{x}} + \left.\frac{h_1^2}{24}\frac{\partial^2}{\partial \xi^2}\right|_{\mathbf{x}} + \left.\frac{h_2^2}{24}\frac{\partial^2}{\partial \eta^2}\right|_{\mathbf{x}}\right)\tilde{\mathbf{v}} = \bar{\mathbf{v}}(\mathbf{x}) \tag{39}
$$

which involves only second spatial derivatives, multiplied by second-order terms. In such a case, having fixed $m=2$, Equation (39) is approximated up to $O(h_1^{m+2}, h_2^{m+2}) = O(h_1^4, h_2^4)$ terms. However, its congruent discretization is not a trivial issue, since the analysis of the local truncation error in the physical space does not provide, by itself, a clear insight of its accuracy. For this reason, the spectral error distribution must also be examined. In fact, a proper discretization of derivatives could be obtained by just considering second-order central differences. Even though such a discretization is consistent with the global fourth-order local truncation error, it has been experienced by the present authors to affect the accuracy of the numerical solution in the spectral space.

In order to clarify the issue, consider equation (39) in one homogeneous direction, for the velocity component u. When the averaging operation at RHS, that is $\bar{u}(x) = \frac{1}{h}\int_{x-h/2}^{x+h/2} u(x')\,\mathrm{d}x'$, is consistently discretized up to fourth-order accuracy, one gets

$$\sum_{p=-P}^{P} w_p \tilde{u}_{i+p} = \sum_{q=-2}^{2} v_q u_{i+q} \tag{40}$$

being $(v_{-2}, v_{-1}, v_0, v_1, v_2) = (-\frac{1}{96}, \frac{1}{12}, \frac{41}{48}, \frac{1}{12}, -\frac{1}{96})$ and $\tilde{u}_i$ standing for the discretized deconvolved field. By using a second-order approximation for the second derivative at LHS, it holds $P = 1$ and $(w_{-1}, w_0, w_1) = (\frac{1}{24}, \frac{11}{12}, \frac{1}{24})$.

Actually, this approximation does not exploit the maximum available grid resolution, since it employs only three of the five nodes involved in the fourth-order flux reconstruction. For this reason, one guesses that a better discretization could be obtained by using the fourth-order accurate central difference formula, for which $P = 2$ and the weights are $(w_{-2}, w_{-1}, w_0, w_1, w_2) = (-\frac{1}{288}, \frac{1}{18}, \frac{43}{48}, \frac{1}{18}, -\frac{1}{288})$.

Hence, the discrete filter implicated in the present method, is a symmetric Pade-type filter, its transfer function resulting in

$$\hat{G}(kh) = \left(\frac{41}{48} + \frac{\cos kh}{6} - \frac{\cos 2kh}{48}\right) \Big/ \left(\frac{11}{12} + \frac{\cos kh}{12}\right) \tag{41}$$

or

$$\hat{G}(kh) = \left(\frac{41}{48} + \frac{\cos kh}{6} - \frac{\cos 2kh}{48}\right) \Big/ \left(\frac{43}{48} + \frac{\cos kh}{9} - \frac{\cos 2kh}{144}\right) \tag{42}$$

for second- and fourth-order accurate formula, respectively. In these definitions, the filter functions are truncated at the Nyquist wave number π/h corresponding to the numerical grid. The transfer functions are plotted in Figure 2, together with those obtained for $m = 0$, by considering both second- and fourth-order integral discretization, i.e. the trapezoidal and the Simpson quadrature rules, respectively. Let us highlight that, owing to the constraint for which the measure h of the FV corresponds to the effective filter width, the continuous top-hat filter is $\hat{T}(kh) = \sin(kh/2)/(kh/2)$, so that the continuous counterpart of (42) is $\hat{G}(kh) = (1 + (k^2h^2/24))\hat{T}(kh)$, as reported in Reference [19]. By making a comparison with the corresponding sharp cut-off filter, it is evident that: (i) whatever discretization order is used, the deconvolution effectively acts for recovering the contribution from smallest resolved scales and (ii) the consistent fourth-order filtering formula (42) improves the result of formula (41). The higher spectral accuracy, herein theoretically illustrated, will be further demonstrated in Section 5 for a practical simulation.

Moreover, the discrete filter (42) has vanishing moments up to third order, reflecting the fact that it is a good approximation to the sharp cut-off filter, which is more appealing according to several authors (e.g. References [21–23]).

It is worth stressing that the deconvolution-based method can be also viewed in the framework of reconstruction procedures for high order FV methods, also referred to as mass matrix construction (e.g. References [13, 14, 19, 28]). However, each assumption about the underlying functional form of the solution would produce a different discrete operator, the spectral resolution of which should be analysed.

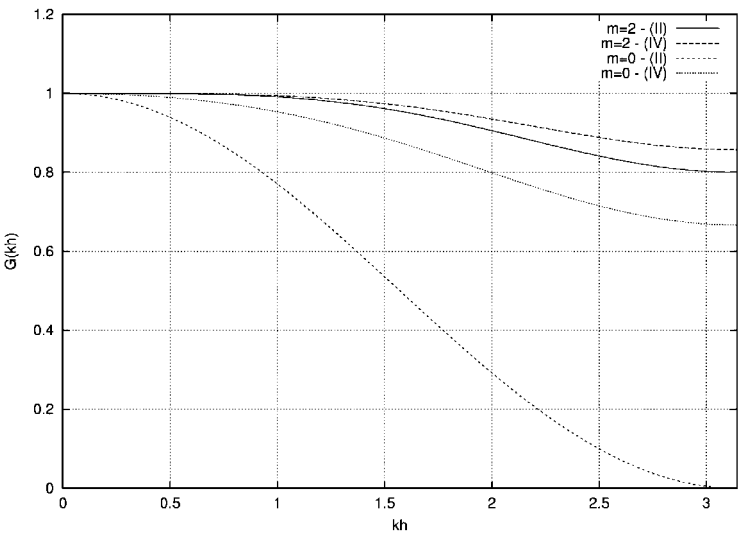

Figure 2. Discrete filter transfer functions. Case $m = 0$: trapezoidal (II) and Simpson (IV) integration. Case $m = 2$: second (II) and fourth-order (IV) FD discretization for the deconvolution operator.

Finally, it can be remarked that the deconvolution does not increase the computational cost of the overall numerical procedure since, due to the adopted semi-implicit time discretization, one simultaneously accounts for both deconvolution and time integration.

3.4. High-order boundary conditions assignment

In solving the prediction equation (14), the assignment of proper boundary conditions is not a trivial task, since the provisional field $\mathbf{v}^*$ does not correspond to the true solution at any intermediate time (e.g. Reference [29]). Actually, by solving the projection equation (16) along with the boundary conditions (17), the normal velocity component on the boundary is exactly satisfied at the new time level, whatever $\mathbf{v}_b^*$ has been prescribed in (14). The same is not true for the tangential velocity component which, evaluated according to (15), results only in an approximation of the physical condition $\mathbf{t} \cdot \mathbf{v}_b^{n+1}$ (e.g. References [26, 30]). However, intermediate boundary conditions can be derived from the knowledge of the variables at previous time levels. For example, in order to improve the accuracy obtained by simply fixing $\mathbf{v}_b^* = \mathbf{v}_b^{n+1}$, some authors interpreted the provisional velocity as a time-continuous field and exploited a truncated Taylor-series expansion, so obtaining $\mathbf{v}_b^* = \mathbf{v}_b^{n+1} + \Delta t \nabla \phi^n|_b$ [25]. As a matter of fact, since the projection step enforces $\partial\phi^{n+1}/\partial n = \partial\phi^n/\partial n = \cdots = \partial\phi^0/\partial n$ at the boundary, a numerical boundary layer is generated, resulting in a reduced effective accuracy of the method. The strategy of resetting, at the end of each time step, the tangential component to its correct physical value was proved to remain still inadequate, as well as it can reduce the smoothness of the velocity field [26, 30].

In order to avoid the use of approximations for the pressure gradient along the boundary, a new proposal for assigning accurate BCs, based solely on the velocity field, is herein derived. That is, by considering Equation $(14)_1$ in the limit for vanishing mesh size and evaluating it

on the boundary, one obtains

$$\left(I - \frac{\Delta t}{2Re}\frac{\partial^2}{\partial y^2}\right)\mathbf{v}^*\Big|_{\partial V} = \left(I + \frac{\Delta t}{2Re}\frac{\partial^2}{\partial y^2}\right)\mathbf{v}^n\Big|_{\partial V} - \left[\frac{\Delta t}{2}\underline{\nabla}\cdot(3\mathbf{v}^n\mathbf{v}^n - \mathbf{v}^{n-1}\mathbf{v}^{n-1}) - \frac{\Delta t}{2Re}\left(3\frac{\partial^2\mathbf{v}^n}{\partial x^2} - \frac{\partial^2\mathbf{v}^{n-1}}{\partial x^2}\right)\right]\Big|_{\partial V} \tag{43}$$

since the truncated deconvolution operator tends toward the identity. Such equation, discretized by means of fourth-order asymmetric FD formulas, is resolved in coupling with the prediction equation, by avoiding the explicit assignment of $\mathbf{v}_b^*$. Such a procedure has been tested for several cases and revealed to fulfill second-order accuracy all the way up to the boundary [36, 37].

As far as the pressure equation is concerned, in solving Equation (16) with the boundary condition (17), it is not necessary to effectively prescribe the normal gradient, the difference $(\partial\phi/\partial n - \mathbf{n}\cdot\mathbf{v}_b^*) = -\mathbf{n}\cdot\mathbf{v}_b^{n+1}$ being known. In fact, by rewriting Equation (16) for the generic FV, one has

$$\int_{y_j^-}^{y_j^+}\left(\frac{\partial\phi}{\partial\xi}\Big|_{x_i^+} - \frac{\partial\phi}{\partial\xi}\Big|_{x_i^-}\right)\mathrm{d}\eta + \int_{x_i^-}^{x_i^+}\left(\frac{\partial\phi}{\partial\eta}\Big|_{y_j^+} - \frac{\partial\phi}{\partial\eta}\Big|_{y_j^-}\right)\mathrm{d}\xi = \int_{y_j^-}^{y_j^+}[u^*(x_i^+,\eta) - u^*(x_i^-,\eta)]\,\mathrm{d}\eta + \int_{y_i^-}^{y_i^+}[v^*(\xi,y_i^+) - v^*(\xi,y_i^-)]\,\mathrm{d}\xi \tag{44}$$

and considering the faces x_i^+ and y_j^- to coincide with a portion of the frontier ∂V where, for example, $u_b^{n+1}(x_i^+, y) = v_b^{n+1}(x, y_j^-) = 0$ are prescribed, the use of (17) leads to

$$\int_{x_i^-}^{x_i^+}\frac{\partial\phi}{\partial\eta}\Big|_{y_j^+}\mathrm{d}\xi - \int_{y_j^-}^{y_j^+}\frac{\partial\phi}{\partial\xi}\Big|_{x_i^-}\mathrm{d}\eta = \int_{x_i^-}^{x_i^+}v^*(\xi,y_j^+)\,\mathrm{d}\xi - \int_{y_j^-}^{y_j^+}u^*(x_i^-,\eta)\,\mathrm{d}\eta \tag{45}$$

In particular, when the Simpson formula is applied to each term of (45), one gets:

$$\frac{h_1}{6}\left(\frac{\partial\phi}{\partial y}\Big|_{i^-,j^+} + 4\frac{\partial\phi}{\partial y}\Big|_{i,j^+}\right) - \frac{h_2}{6}\left(4\frac{\partial\phi}{\partial x}\Big|_{i^-,j} + \frac{\partial\phi}{\partial x}\Big|_{i^-,j^+}\right) = \frac{h_1}{6}(v^*_{i^-,j^+} + 4v^*_{i,j^+}) - \frac{h_2}{6}(4u^*_{i^-,j} + u^*_{i^-,j^+}) \tag{46}$$

Such equation is discretized in space by means of proper asymmetric FD formulas and without using ghost-points.

4. THE DECONVOLUTION-BASED FV METHOD IN THE LES FRAMEWORK

In this section, the present deconvolution-based FV method is interpreted from the LES point of view. In this framework, Equation (3) defines the filtered velocity as resulting from the filtering operation $\bar{\mathbf{v}} = G * \mathbf{v}$, G being the top-hat filter kernel so that the integral momentum equation (2) can be formally rewritten as the explicitly top-hat filtered NS equation:

$$\frac{\partial \bar{\mathbf{v}}}{\partial t} + G * [\underline{\nabla} \cdot \mathbf{F}(\mathbf{v})] = \mathbf{0} \tag{47}$$

The corresponding LES momentum equation is

$$\frac{\partial \bar{\mathbf{v}}}{\partial t} + G * [\underline{\nabla} \cdot \mathbf{F}(\bar{\mathbf{v}})] = G * (\underline{\nabla} \cdot \mathbf{T}) \tag{48}$$

having defined the filtered momentum flux tensor as $\mathbf{F}(\bar{\mathbf{v}}) = \bar{\mathbf{v}}\bar{\mathbf{v}} + \mathbf{I}p - (1/Re)(\underline{\nabla}\bar{\mathbf{v}} + \underline{\nabla}^{\mathrm{T}}\bar{\mathbf{v}})$. Let us notice that Equation (48) holds for general non-uniform filtering, since the commutativity between filtering and differentiation is not therein required. The SGS stress tensor $\mathbf{T}$ is defined according to

$$\mathbf{T} = (\bar{\mathbf{v}}\bar{\mathbf{v}} - \mathbf{v}\mathbf{v}) - \frac{2}{Re}(\bar{\mathbf{S}} - \mathbf{S}) \tag{49}$$

and must be modelled in order to close the LES problem in the unknown $\bar{\mathbf{v}}$. In Equation (49), $\mathbf{S} = \frac{1}{2}(\underline{\nabla}\mathbf{v} + \underline{\nabla}^{\mathrm{T}}\mathbf{v})$ stands for the velocity strain-rate tensor as well as $\bar{\mathbf{S}} = \frac{1}{2}(\underline{\nabla}\bar{\mathbf{v}} + \underline{\nabla}^{\mathrm{T}}\bar{\mathbf{v}})$. In deriving Equation (48), the filtering operation is explicitly indicated as it corresponds to the actual FV integration. Let us point out that the SGS term at RHS of Equation (48) preserves a non-local character, but in approximating (49) one can also use models which are local in space, the introduction of additional explicit filtering operation (as proposed, for instance, in Reference [38]) not being required. Indeed, in FV simulations, it appears suitable to use the SGS stress definition (49), where the convective term is not explicitly filtered, the further filtering operation being involved by the volume integration. Moreover, a diffusive term was also correctly considered.

As a matter of fact, methods based upon a truncated Taylor-series expansion has been exploited in deriving turbulence models since the pioneering work by Leonard [39], while approximate deconvolution procedures have been recently exploited for developing SGS modeling procedures [32–35]. In this context, according to the approximate deconvolution model (ADM) [34, 35], Equation (49) could be approximated as

$$\mathbf{T} \cong (\bar{\mathbf{v}}\bar{\mathbf{v}} - \tilde{\mathbf{v}}\tilde{\mathbf{v}}) - \frac{2}{Re}(\bar{\mathbf{S}} - \tilde{\mathbf{S}}) \tag{50}$$

where $\tilde{\mathbf{S}} = \frac{1}{2}(\underline{\nabla}\tilde{\mathbf{v}} + \underline{\nabla}^{\mathrm{T}}\tilde{\mathbf{v}})$ stands for the high-order filtered velocity strain-rate tensor.

Alternatively, according to the generalized scale similarity (GSS) model [32, 33], one has

$$\mathbf{T} \cong (\bar{\tilde{\mathbf{v}}}\bar{\tilde{\mathbf{v}}} - \tilde{\mathbf{v}}\tilde{\mathbf{v}}) - \frac{2}{Re}(\bar{\tilde{\mathbf{S}}} - \tilde{\mathbf{S}}) \tag{51}$$

where $\bar{\tilde{\mathbf{S}}} = \frac{1}{2}(\underline{\nabla}\bar{\tilde{\mathbf{v}}} + \underline{\nabla}^{\mathrm{T}}\bar{\tilde{\mathbf{v}}})$. In both (50) and (51) $\tilde{\mathbf{v}}$ stands for the approximately deconvolved velocity, that is

$$\tilde{\mathbf{v}} \equiv G_{\mathrm{inv}}^{(m)} * \bar{\mathbf{v}} \tag{52}$$

$G_{\mathrm{inv}}^{(m)}$ being an mth order approximate inverse of G. However, as it is well known since their inception, scale-similarity models, though exhibiting high-level correlation in *a priori* tests, nevertheless they are only slightly dissipative and need to be supplied with an eddy viscosity SGS term, that leads to the adoption of mixed models [40]. For instance, by supplying model (51) with the Smagorinsky eddy-viscosity model, one obtains

$$\mathbf{T} \cong (\bar{\tilde{\mathbf{v}}}\bar{\tilde{\mathbf{v}}} - \tilde{\mathbf{v}}\tilde{\mathbf{v}}) - \frac{2}{Re}(\bar{\tilde{\mathbf{S}}} - \tilde{\mathbf{S}}) + 2(C\Delta)^2|\bar{\mathbf{S}}|\bar{\mathbf{S}} \tag{53}$$

where $|\bar{\mathbf{S}}|$ stands for the magnitude of the averaged velocity strain-rate tensor, C stands for a model coefficient and the filter width Δ corresponds to the linear extent of the FV. A similar mixed model can be derived starting from Equation (50).

These modelling procedures, based upon the approximate deconvolution of the volume-averaged velocity, are now extended to the present FV methodology. This task requires the proper definition of the numerical flux function according to (49), as well as the explicit discrete convolution of the SGS term. To the authors' knowledge, such an extension has not been presented elsewhere.

As far as the present procedure is concerned, by considering definition (52) one has $A_x^{(m)}(\,) = G_{\mathrm{inv}}^{(m)} * (\,)$. By defining the high-order filtering operation $\tilde{\mathbf{v}} = G_{\mathrm{inv}}^{(m)} * [G * \mathbf{v}]$, the governing equation (6) can be formally rewritten as the high-order filtered NS equation

$$\frac{\partial \tilde{\mathbf{v}}}{\partial t} + G_{\mathrm{inv}}^{(m)} * \{G * [\underline{\nabla} \cdot \mathbf{F}(\mathbf{v})]\} = \mathbf{0} \tag{54}$$

Hence, the corresponding LES momentum equation for the unknown $\tilde{\mathbf{v}}$ becomes

$$\frac{\partial \tilde{\mathbf{v}}}{\partial t} + G_{\mathrm{inv}}^{(m)} * \{G * [\underline{\nabla} \cdot \mathbf{F}(\tilde{\mathbf{v}})]\} = G_{\mathrm{inv}}^{(m)} * [G * (\underline{\nabla} \cdot \mathbf{T}^{(m)})] \tag{55}$$

that can be recast in a form corresponding to Equation (8) by writing

$$[G_{\mathrm{inv}}^{(m)}]^{-1} * \frac{\partial \tilde{\mathbf{v}}}{\partial t} + G * [\underline{\nabla} \cdot \mathbf{F}(\tilde{\mathbf{v}})] = G * (\underline{\nabla} \cdot \mathbf{T}^{(m)}) \tag{56}$$

in which the SGS term is now defined according to

$$\mathbf{T}^{(m)} = (\tilde{\mathbf{v}}\tilde{\mathbf{v}} - \mathbf{v}\mathbf{v}) - \frac{2}{Re}(\tilde{\mathbf{S}} - \mathbf{S}) \tag{57}$$

This definition, as well as the effective importance of $\mathbf{T}^{(m)}$, strongly depends on the adopted filter width, corresponding to the FV grid size, as well as on its shape, corresponding to the fixed deconvolution order m [19, 22, 41]. Observe that, when modelled according to the only ADM procedure (i.e. $\mathbf{v} \cong \tilde{\mathbf{v}}$), the unknown SGS stresses (57) identically vanish. In this case, the governing equation (55) closely resembles the evolution equation for the approximately deconvolved velocity considered in References [31, 34, 35].

Alternatively, according to the GSS mixed model, it holds instead that

$$\mathbf{T}^{(m)} \cong (\tilde{\tilde{\mathbf{v}}}\tilde{\tilde{\mathbf{v}}} - \tilde{\mathbf{v}}\tilde{\mathbf{v}}) - \frac{2}{Re}(\tilde{\tilde{\mathbf{S}}} - \tilde{\mathbf{S}}) + 2(C\Delta)^2|\tilde{\mathbf{S}}|\tilde{\mathbf{S}} \tag{58}$$

where, obviously, $\tilde{\tilde{\mathbf{S}}} = \frac{1}{2}(\underline{\nabla}\tilde{\tilde{\mathbf{v}}} + \underline{\nabla}^{\mathrm{T}}\tilde{\tilde{\mathbf{v}}})$. It is worth remarking that, for a given filter width, by increasing the deconvolution order m, the high-order filtered velocity (52) tends towards the spectral cut-off counterpart for which the scale similarity part of the model would vanish.

5. NUMERICAL RESULTS

In this section, by exploiting an exact NS solution, the high space–time accuracy of the presented FV method is first examined. This kind of flow is often considered for validating unsteady NS solvers (e.g. References [16, 25]). Then, in order to investigate the capabilities of the present method in simulating real flows, a time evolving mixing layer solution is carried out in the context of both DNS and LES approaches.

5.1. Accuracy analysis

The adopted test case for the accuracy analysis is the following 2-D Taylor solution:

$$\begin{aligned} u(x, y, t) &= -\cos x \sin y \mathrm{e}^{-2t} \\ v(x, y, t) &= \sin x \cos y \mathrm{e}^{-2t} \\ p(x, y, t) &= -0.25(\cos 2x + \cos 2y)\mathrm{e}^{-4t} \end{aligned} \tag{59}$$

depicting a decaying vortex interaction. The velocity field is initialized by making use of (59) in the domain $V = [-\pi, \pi) \times [-\pi, \pi)$. When non-uniform grids are considered, a cosine-based stretching law is adopted in y-direction (the refinement being performed around $y = 0$), while retaining a uniform grid spacing in x-direction. The discretization error is evaluated by taking the L_∞ norm of the difference between the exact and the computed u fields, that appears to be the most meaningful way to study the local accuracy of the method.

The spatial accuracy is analysed by fixing $\Delta t = 10^{-4}$ and computing the errors after 100 time steps for two different types of boundary conditions. In Figure 3, the effect of the deconvolution procedure is studied for the homogeneous case, by imposing periodical boundary conditions along each direction. The results, for both uniform and non-uniform grids, are reported in terms of the discretization errors against the normalised mesh size, that is the ratio between the actual and the smallest adopted grid spacing. It clearly appears how, in presence of the de-averaging procedure ($m = 2$), a fourth-order convergence is successfully obtained, confirming that the step-by-step deconvolution provides a fourth-order approximation to the point-wise field. On the contrary, in absence of the deconvolution ($m = 0$), one obtains only a second-order accurate solution, regardless of using a fourth-order flux reconstruction. In order to validate the spatial discretization of Equation (43), a simulation has been performed by prescribing Dirichlet boundary conditions at $y = \pm\pi$, while retaining the periodic ones at $x = \pm\pi$. The fourth-order spatial accuracy is still maintained all the way up to the boundary, as illustrated in Figure 4.

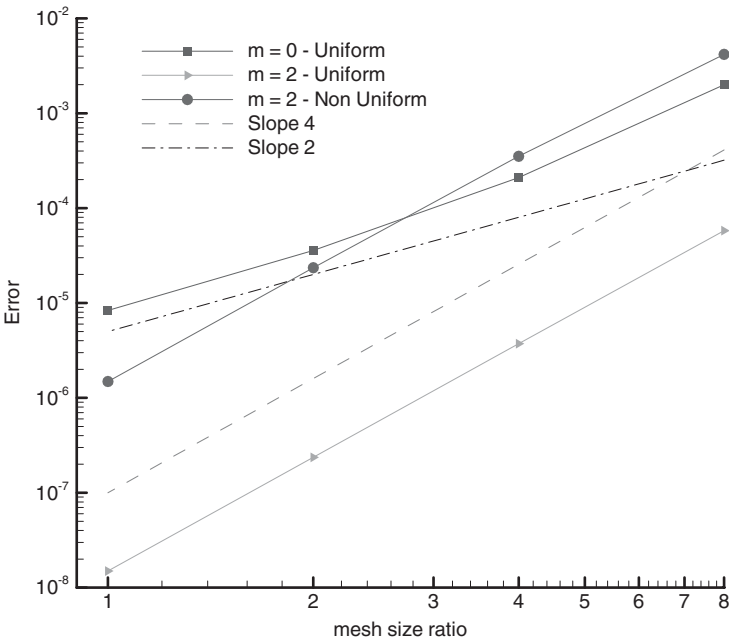

Figure 3. Effect of the de-convolution on the spatial accuracy for the homogeneous case. The errors are computed after 100 time steps on both uniform and non-uniform grids.

Finally, the time accuracy of the present FTS method has been examined. The discretization error has been evaluated after a single time step integration, on a 60×60 mesh. As expected, thanks to the high-order intermediate boundary conditions, a third-order slope has been obtained, see Figure 5, corresponding to a second-order local truncation error. Conversely, it was experienced that the adoption of intermediate boundary conditions based upon Taylor-series expansion proposed in Reference [25] leads to a first-order truncation error.

5.2. Time evolving mixing layer

Although it could be debatable the mixing layer represents a model of real turbulent flow, nevertheless it can be considered a good model problem for testing high-order numerical methods for unsteady incompressible flows. In fact, this flow exhibits the non-linear development of Kelvin–Helmholtz instabilities in which vorticity dynamics play a fundamental role [42]. This complex dynamics is strongly sensitive to the truncation error associated to the numerical method and mixing layer simulations are currently conducted, also at moderate Reynolds numbers, in order to address the main features of a numerical method (e.g. Reference [43]).

5.2.1. Model-free simulation. The aim of this section is to show the good spectral resolution obtained by means of the proposed deconvolution-based FV method. In order to have a meaningful comparison between different numerical methods, we assume all the reported solutions to correspond to the same characteristic time, say T, as later specified. Numerical simulations are carried out in the domain $V = [0, 4\lambda_a) \times [-2\lambda_a, 2\lambda_a]$, $\lambda_a = 7\delta_1$ being an approximation

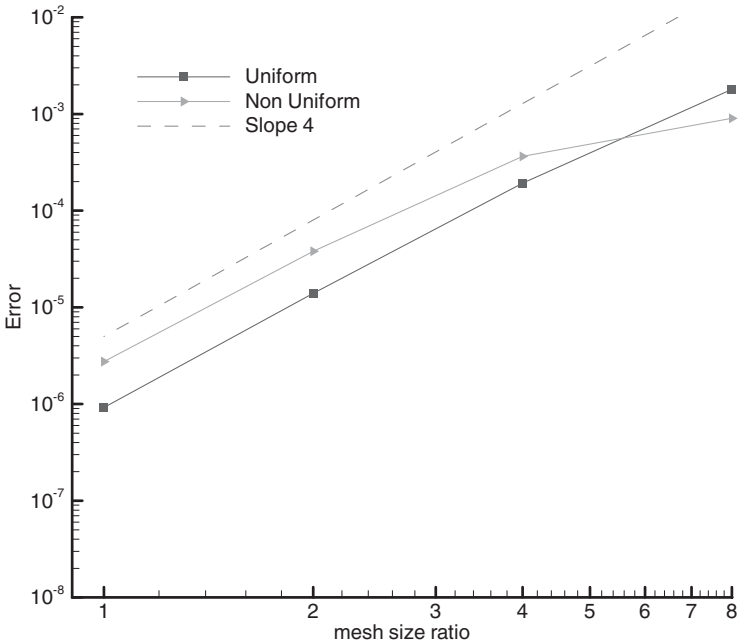

Figure 4. Space accuracy analysis for the non-homogeneous case. The errors are computed after 100 time steps on both uniform and non-uniform grids.

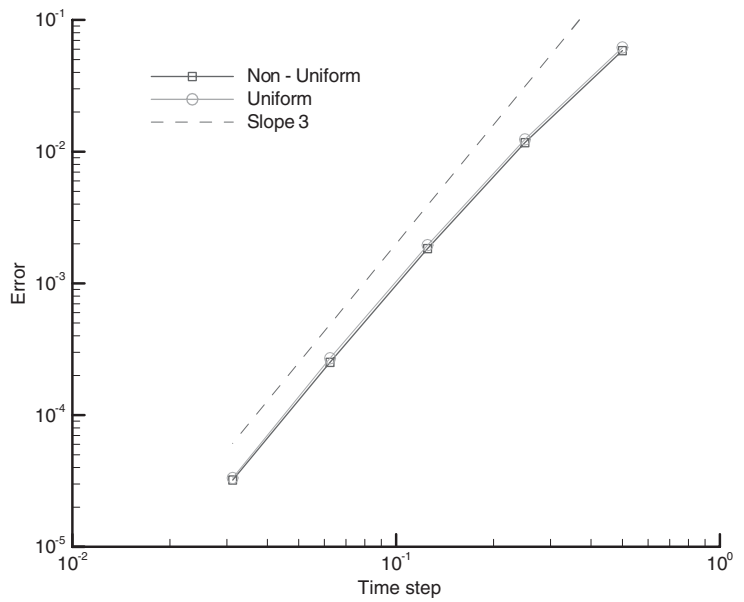

Figure 5. Time accuracy analysis. The errors are computed after one time step on both uniform and non-uniform 60×60 grids.

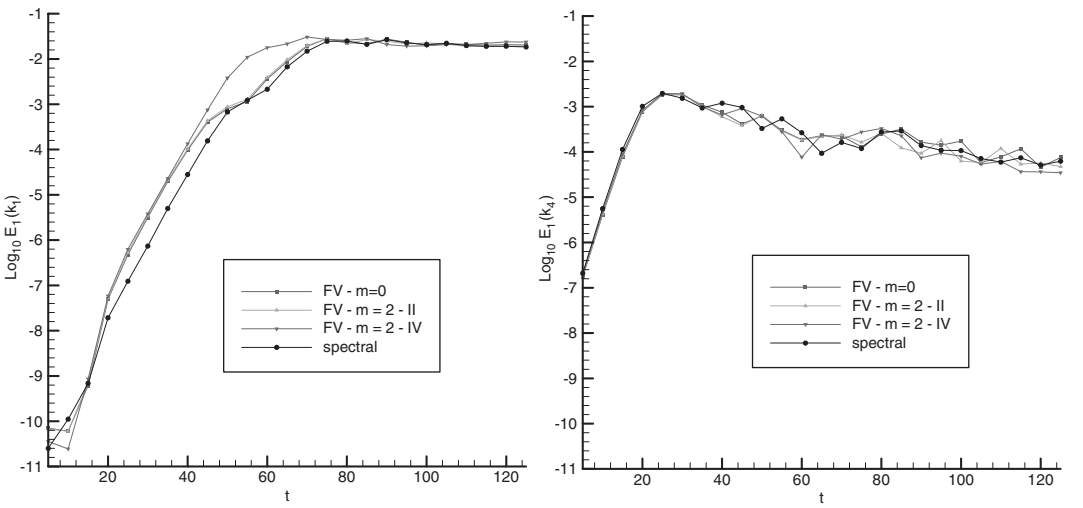

Figure 6. Mixing layer model-free simulation: time evolution of the energy associated to the characteristic wave numbers k_1 (left) and k_4 (right), for different FV simulations on a 128×128 uniform grid, along with the reference spectral solution.

of the most unstable wavelength in the homogeneous x-direction and δ_1 the initial vorticity thickness. The same initial velocity profile adopted in Reference [42] is here considered, that is $u(y) = u_\infty \tanh 2y/\delta_1$, u_∞ being the asymptotic velocity. Both a deterministic sine perturbation at the wave number $k_4 = 2\pi/\lambda_a$ and a white noise are superimposed upon the initial velocity field, in order to trigger and tune the instability. Moreover, free-stream conditions are prescribed at $y = \pm 2\lambda_a$ while the Reynolds number is fixed to $Re = u_\infty \delta_1/\nu = 500$. For our purposes, results are provided in terms of the one-dimensional longitudinal energy spectrum for the streamwise velocity component

$$E_1(k) \equiv \frac{1}{4\lambda_a} \int_{-2\lambda_a}^{2\lambda_a} |\hat{u}(k, y)|^2 \, \mathrm{d}y$$

$\hat{u}$ being the 1-D Fourier transform of u along the x-direction.

In the following, a spectral solution, obtained on a computational domain doubled in y-direction, is used as a reference. In this respect, a 384×768 modes resolution has been proved to be sufficient for obtaining a grid independent solution. As a first result, the time evolution of $E_1(k_1)$ and $E_1(k_4)$, $k_1 = k_4/4$ being the characteristic wave number associated with the largest vortex, for fixed longitudinal extent of the computational domain, is reported in Figure 6. Results from different FV simulations on a 128×128 uniform grid for a fixed non-dimensional $\Delta t = 10^{-3}$, as well as those ones obtained by means of the spectral method, are shown. It clearly appears that $120\delta_1/u_\infty$ is quite a good choice for the characteristic time T. In fact, at this time, after a slightly different transient, all solutions tend toward the same energy level. In particular, the FV results are obtained from simulations performed with and without deconvolution, the former being carried out with both second (II) and fourth-order (IV) FD approximations for the second derivatives in the deconvolution operator, as discussed in Section 3.3.3.

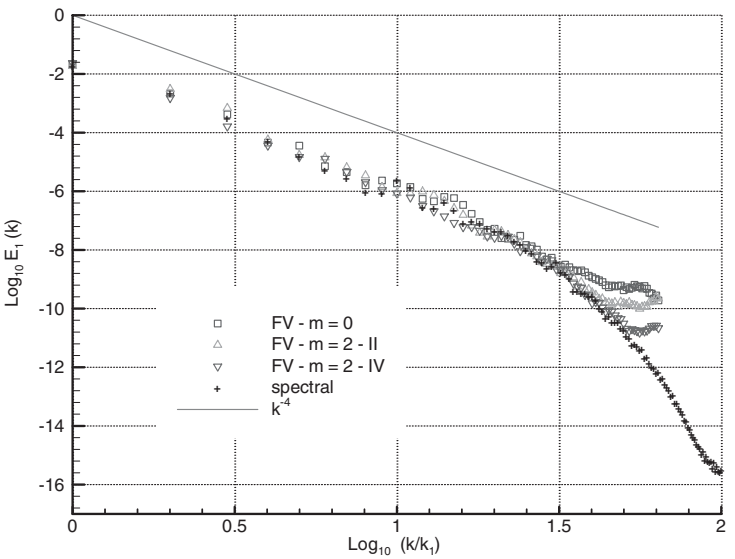

Figure 7. Mixing layer model-free simulation: energy spectra for different solutions on a 128×128 uniform grid, with ($m = 2$) and without ($m = 0$) deconvolution. The former with second (II) and fourth-order (IV) FD discretization for the deconvolution operator. The spectral reference solution is also reported.

The effectiveness of both deconvolution and its proper discretization are clearly demonstrated in Figure 7, where the energy spectra at time T, corresponding to different numerical solutions, are reported. In particular, the highest order discretization of the deconvolution operator provided the best resolution, allowing for a well resolved wave numbers range about 60 per cent larger with respect to the case $m = 0$. Though no SGS model has been explicitly used, this result demonstrates how the present high-order deconvolution-based FV method allows us to properly describe most of the resolved wave number components of the flow. This also holds for the actual grid, which does not allow for a real DNS solution. As already discussed in Section 4, this is in accordance to having a sort of implicit turbulence modelling. The effect of the deconvolution is also evident after inspection of Figure 8, where the iso-vorticity contours at the same time T, corresponding to the non-dimensional levels 0.1, 0.15 and 1, are drawn. Indeed, for $m = 0$, contrarily to $m = 2$, some oscillations appear in the vorticity field, reflecting the presence of significant residual energy at highest resolved wave numbers, as already illustrated in Figure 7.

Furthermore, by adopting a cosine stretching law along the y-axis while maintaining the same number of FVs along each direction, the effect of using a non-uniform cell distribution is examined. The resulting longitudinal energy spectra are drawn in Figures 9 and 10, for the cases $m = 0$ and 2, respectively. In the former case, the effectiveness of grid stretching in increasing the spectral resolution of the computed velocity field is quite clear. The gain is less evident in the latter case, since the deconvolution already allows recovering the most part of the highest resolved wavenumber components. In fact, for the actual coarse DNS, it appears that either grid stretching or deconvolution produce similar good effect. By making a comparison between Figures 9 and 10, one can conclude that the best spectral resolution is

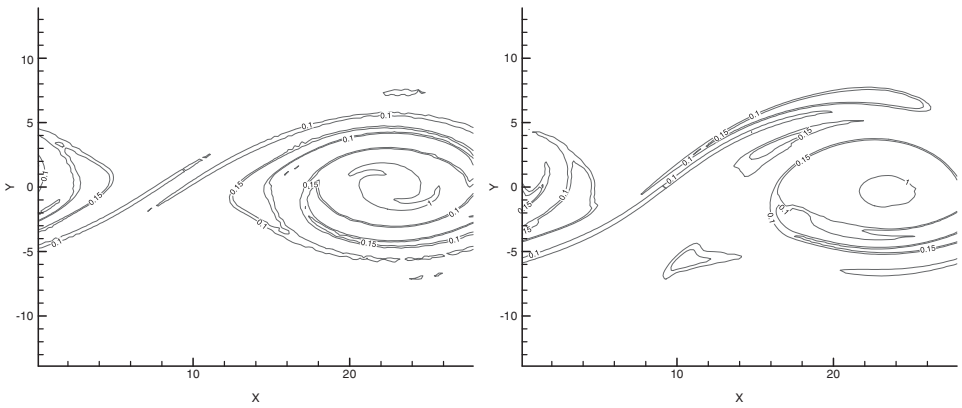

Figure 8. Mixing layer model-free simulation: iso-vorticity contours $(0.1, 0.15, 1)$ corresponding to the cases $m = 0$ (left) and $m = 2$ (right) with a fourth-order FD discretization for the deconvolution operator.

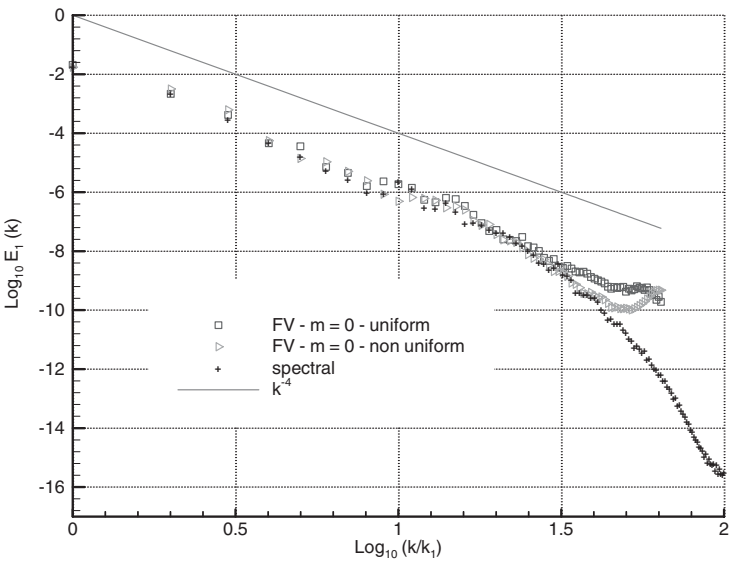

Figure 9. Mixing layer model-free simulation: energy spectra for FV solutions on a 128×128 grid, corresponding to $m = 0$, with and without grid stretching. The spectral reference solution is also reported.

obtained by virtue of the deconvolution procedure. However, these conclusions could depend on the actual flow conditions and the issue must be better examined in future works, by simulating real 3-D turbulent flows.

Finally, for a sufficiently fine grid, the present methodology led to a solution resembling the spectral one. Actually, the result obtained on a 256×256 uniform grid, reported in Figure 11, can be considered as a DNS solution since a further refinement showed no significant improvement.

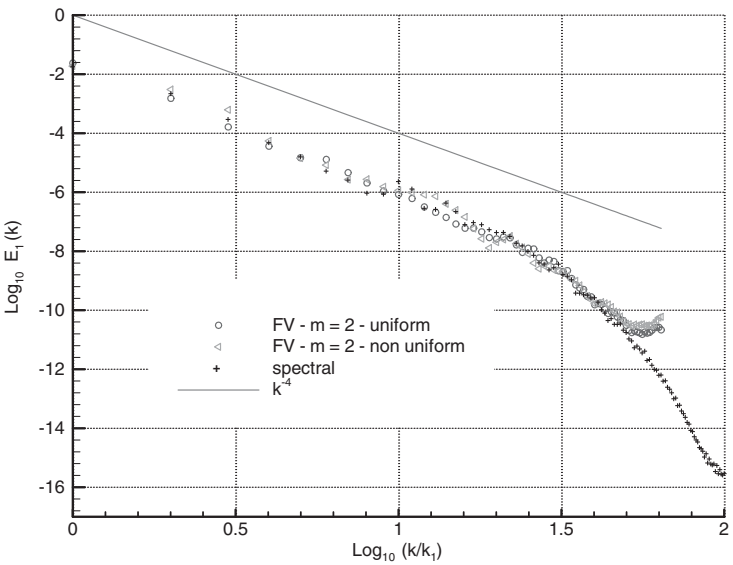

Figure 10. Mixing layer model-free simulation: energy spectra for FV solutions on a 128×128 grid, corresponding to $m = 2$, with and without grid stretching. The spectral reference solution is also reported.

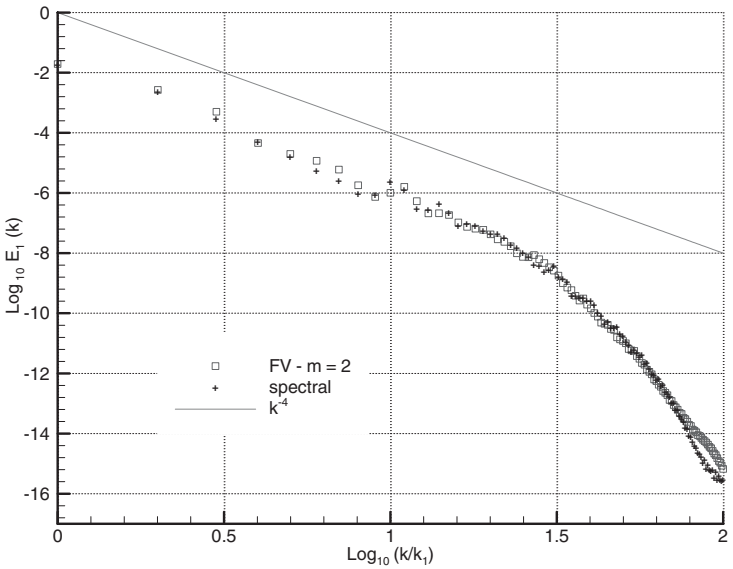

Figure 11. Mixing layer model-free simulation: energy spectra corresponding to a FV solution on a 256×256 uniform grid, for $m = 2$. The spectral reference solution is also reported.

5.2.2. Modelled simulation. So far, the evolution equation $(9)_2$ has been solved without introducing any explicit SGS model, that is by fixing $\mathbf{T}^{(2)} = \mathbf{0}$ as it results by adopting the ADM approximation in Equation (57). This is also equivalent to solving Equation (48) for

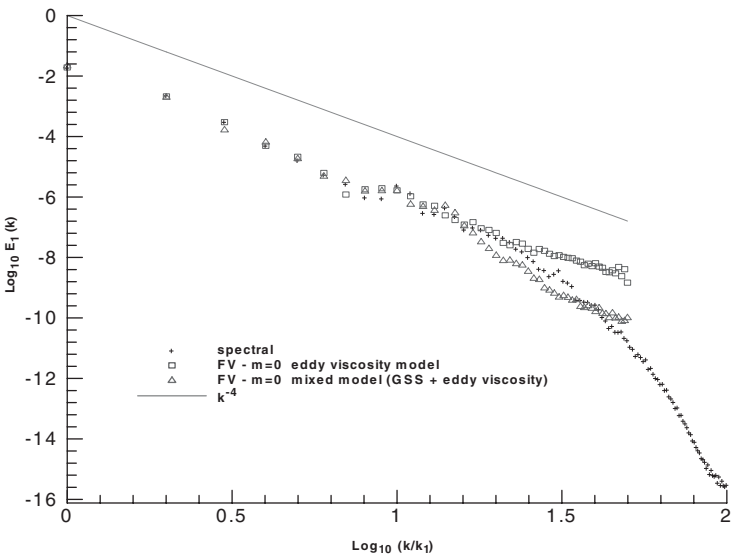

Figure 12. Mixing layer modelled simulation: energy spectra corresponding to a FV solution on a 100×100 uniform grid, for $m = 0$ and different SGS models. The spectral reference solution is also reported.

the top-hat filtered velocity, supplied with the ADM expression (50), as also recognized in Reference [34].

In this section, some preliminary results about the implementation of the present high-order method for LES of incompressible turbulent flows are presented. In order to close the evolution equations for the filtered velocity, mixed SGS models based upon the eddy viscosity Smagorinsky model have been used. The coefficient for the Smagorinsky model has been fixed to $C = 0.04$ for all simulations. A coarse 100×100 grid is used for the domain discretization. The time integration of the modelled SGS terms is performed by means of the explicit AB scheme and the intermediate boundary condition (43) is appropriately modified by including the model.

First, without performing the deconvolution of the volume-averaged velocity ($m = 0$), the LES equation (48) has been solved with the mixed model based upon both the ADM (50) and the GSS model (51). It has been found that the LES supplied with the former becomes unstable while the latter provides the result reported in Figure 12. The solution obtained by exploiting the sole Smagorinsky model is also shown in the same figure, confirming the superior performances of the GSS mixed model with respect to the pure eddy-viscosity one. However, in this case, the chosen value for the Smagorinsky constant appears to be too high, leading to an over-estimated energy dissipation. The better behaviour of the LES based upon (51) might be due to the fact that the highest frequencies are somehow smoothed by the double filtering operation. However, all these features might also depend on the explicit AB time integration of the SGS terms and, thus, such issue requires some more study. Anyway, these results prove both the correctness and the accuracy of the present formulation, as an extension of the deconvolution-based SGS modelling to the FV approach.

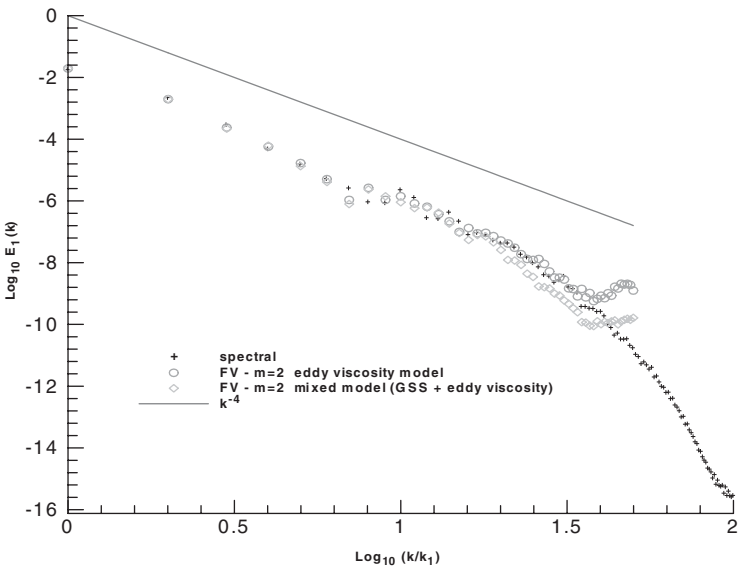

Figure 13. Mixing layer modelled simulation: energy spectra corresponding to a FV solution on a 100×100 uniform grid, for $m = 2$ and different SGS models. The spectral reference solution is also reported.

Then, as far as the LES in terms of the deconvolved velocity is concerned ($m = 2$), Equation (56) is solved by means of both the mixed model (58) and the pure Smagorinsky one. Owing to the step-by step deconvolution, the simulation remains stable also in the latter case. The results are presented in Figure 13 and once again demonstrate the capability of the present high-order FV method to accurately represent the energy transfer at highest frequencies. However, the mixed model remains too dissipative, that is not surprising since part of the dissipation is already provided by the scale-similarity model and the Smagorinsky constant should be correspondently adjusted. Actually, the simulations could be improved by determining this coefficient by means of a dynamic procedure, that will be a subject of future work. As a final test, a simulation without any modelling has been done also for this coarse grid, providing an unstable solution.

From the observation of Figures 12 and 13, the smallest resolved scales appear to be contaminated by the truncation errors, resembling the shape of the transfer functions reported in Figure 2. By exploiting an additional explicit filtering with $\Delta > h$ one could avoid this problem but a finer grid could be necessary for the same resolution. However, when the GSS model is adopted, the deconvolution-based procedure seems equivalent to solving for the volume-averaged velocity.

6. CONCLUSIONS

This paper was devoted to the development of a real fourth-order accurate FV method for simulating unsteady incompressible viscous flows on non-uniform Cartesian grids. The high

accuracy of the method was accomplished by exploiting both high-order flux integration and a suitable deconvolution procedure for the volume-averaged velocity. Thus, contrarily to other classical high-order FV formulations, the resolved field effectively stands for a fourth-order approximation to the point-wise solution. As FV simulations are much more feasible than the spectral ones for simulating complex flows, the present method, leading to a good resolution in spectral space, appears very efficient.

A classical projection method for the pressure–velocity decoupling of the NS equations system was exploited. In this context, proper intermediate boundary conditions for the prediction step were originally proposed and their implementation provided a real second-order time accuracy solution. The overall high accuracy of the method was demonstrated, for uniform and non-uniform grids, by considering a classical analytical NS solution. Moreover, a 2-D time-evolving mixing layer simulation emphasized the efficacy of the deconvolution procedure, by also addressing the effect of the appropriate discretization of the inverse deconvolution operator.

The present method was also viewed in the context of LES. As the deconvolution procedure allows us to have a good spectral resolution in the resolved wave numbers range, it becomes possible to improve the performances of classical SGS models, since they essentially rely on the smallest resolved scales. On the other hand, it was recognized that the deconvolution acts as a sort of implicit SGS modelling for the filtered NS equations. In this respect, the actual numerical procedure can be cast in the context of approximate deconvolution modelling procedures for LES. However, an explicit dissipation model for the residual stress terms must be added, as clearly confirmed by the mixing layer simulation. Note that the present formulation can be generalized within the framework of the explicit-filtering LES approach in order to keep the numerical and the filtering issues apart. Specifically, once the fourth-order flux integration has been performed, the volume-averaged field can be built on a larger cell, composed of a suitable set of adjacent ones. Consequently, by means of the deconvolution procedure, one obtains a velocity field which is filtered over a characteristic length different from the grid size, thus avoiding the balanced variable being contaminated by numerical errors at highest resolved wave-numbers. However, in order to further address how the present method performs in LES approach, more research is needed.

Finally, according to the general formulation developed in Section 2, the extension of the present procedure to 3-D flow simulations is straightforward. Here, the evaluation of fluxes would require a fourth-order accurate surface integration and a generalization of the interpolation strategy, while the FTS methodology, as well as the implementation of the high-order intermediate boundary conditions, could be easily maintained.

REFERENCES

1. Harlow FH, Welch JE. Numerical calculation of time-dependent viscous incompressible flow of fluid with free surface. *Physics of Fluids* 1965; **8**:2182–2189.
2. Schumann U. Subgrid scale model for finite difference simulations of turbulent flows in plane channels and annuli. *Journal of Computational Physics* 1975; **18**:376–404.
3. Ghosal S. An analysis of numerical errors in Large Eddy Simulations of turbulence. *Journal of Computational Physics* 1996; **125**:187–206.
4. Kravchenko AG, Moin P. On the effect of numerical errors in large eddy simulations of turbulent flows. *Journal of Computational Physics* 1997; **131**:310–322.
5. Rogallo RS, Moin P. Numerical simulation of turbulent flows. *Annual Reviews in Fluid Mechanics* 1984; **16**:99–137.

6. Ghosal S, Moin P. The basic equations for the large eddy simulation of turbulence flows in complex geometry. *Journal of Computational Physics* 1995; **118**:24–37.
7. Morinishi Y, Lund TS, Vasilyev OV, Moin P. Fully conservative higher order finite difference schemes for incompressible flow. *Journal of Computational Physics* 1998; **143**:90–124.
8. Vasilyev OV. High order finite difference schemes on non-uniform meshes with good conservation properties. *Journal of Computational Physics* 2000; **157**:746–761.
9. Castillo J, Hyman JM, Shashkov M, Steinberg S. The Sensitivity and accuracy of fourth order finite-difference schemes on non-uniform grids in one dimension. *International Journal of Computers & Mathematics with Applications* 1995; **30**(8):41–55.
10. Hyman JM, Shashkov M. Natural discretizations for the divergence, gradient, and curl on logically rectangular grids. *International Journal of Computers & Mathematics with Applications* 1997; **33**(4):81–104.
11. Leveque RJ. *Numerical Methods for Conservation Laws*. Birkhauser: New York, 1992.
12. Temam R. Some developments on Navier–Stokes equations in the second half of the 20th century. In *Dévelopment des Mathématiques au cours de la seconde moitié du XXème siécle*, J.P. Pier Managing (ed.). Birkhauser: New York, 1999.
13. Harten A, Engquist B, Osher S, Chakravarty S. Uniformly high order essentially non-oscillatory schemes, III. *Journal of Computational Physics* 1987; **71**:231–243.
14. Liu XD, Osher S, Chan T. Weighted essentially non-oscillatory schemes. *Journal of Computational Physics* 1994; **115**:200–212.
15. Lilek Z, Peric M. A fourth-order finite volume method with colocated variable arrangement. *Computers and Fluids* 1995; **24**:239–252.
16. Pereira JMC, Kobayashi MH, Pereira JCF. A fourth order accurate finite volume compact method for the incompressible Navier–Stokes solutions. *Journal of Computational Physics* 2001; **166**:217–243.
17. Denaro FM. Toward a new model-free simulation of high-Reynolds-flows: Local Average Direct Numerical Simulation. *International Journal for Numerical Methods in Fluids* 1996; **23**:125–142.
18. De Stefano G, Denaro FM, Riccardi G. Analysis of 3-D backward facing step incompressible flows via a local average-based numerical procedure. *International Journal for Numerical Methods in Fluids* 1998; **25**:1073–1091.
19. De Stefano G, Denaro FM, Riccardi G. High order filtering for control volume flow simulations. *International Journal for Numerical Methods in Fluids* 2001; **37**(7):797–835.
20. Sagaut P. *Large Eddy Simulation for Incompressible Flows. An Introduction*. Springer: Berlin, 2001.
21. Lund TS, Kaltenbach H-J. Experiments with explicit filtering for LES using a finite-difference method. *Annals of Research Briefs*, Center for Turbulence Research, 1995.
22. De Stefano G, Vasilyev OV. Sharp cut-off versus smooth filtering in large eddy simulation. *Physics of Fluids* 2002; **14**(1):362–369.
23. Vasilyev OV, Lund TS, Moin P. A general class of commutative filters for LES in complex geometries. *Journal of Computational Physics* 1998; **143**:105–123.
24. Chorin AJ. Numerical Solution of the Navier–Stokes Equations. *Mathematics of Computation* 1968; **22**: 745–762.
25. Kim J, Moin P. Application of a fractional-step method to incompressible Navier–Stokes equations. *Journal of Computational Physics* 1985; **59**:308–323.
26. Brown DL, Cortez R, Minion ML. Accurate projection methods for the incompressible Navier–Stokes equations. *Journal of Computational Physics* 2001; **59**:464–499.
27. van der Ven H. A family of large eddy simulation (LES) filters with nonuniform filter widths. *Physics of Fluids* 1995; **7**(5):1171–1172.
28. Barth TJ, Deconinck H (eds). *High-order methods for computational physics*, Lectures Notes in Computational Science and Engineering. Springer: Berlin, 1999.
29. LeVeque RJ. Intermediate boundary conditions for LOD, ADI and approximate factorization methods, ICASE report no.85-21, NASA Langley Research Center, Hampton, Virginia, 1985.
30. Strikwerda JC, Lee YS. The accuracy of the fractional step method. *SIAM Journal on Numerical Analysis* 1999; **37**(1):37–47.
31. Tadmor E. Convergence of spectral methods for non-linear conservation laws. *SIAM Journal on Numerical Analysis* 1989; **26**:30–44.
32. Shah KB, Ferziger JH. A new non-eddy viscosity subgrid-scale model and its application to channel flow. *Annuals of Research Briefs*, Center for Turbulence Research, 1995.
33. Geurts BJ. Inverse modeling for large-eddy simulation. *Physics of Fluids* 1997; **9**(12):3585–3587.
34. Stolz S, Adams NA. An approximate deconvolution procedure for large-eddy simulation. *Physics of Fluids* 1999; **11**(7):1699–1701.
35. Adams NA, Stolz S. A subgrid-scale deconvolution approach for shock capturing. *Journal of Computational Physics* 2002; **178**:391–426.
36. Denaro FM. On the application of the Helmholtz–Hodge decomposition in projection methods for incompressible flows with general boundary conditions. *International Journal for Numerical Methods in Fluids* 2003; **43**:43–70.

37. Iannelli P, Denaro FM. Analysis of the local truncation error in the pressure-free projection method for the Navier–Stokes equations: a new accurate expression of the boundary conditions. *International Journal for Numerical Methods in Fluids* 2003; **42**:399–437.
38. Horiuti K. Backward scatter of sub-grid scale energy in wall-bounded turbulence and free shear flow. *Journal of Physical Society of Japan* 1997; **66**:91–107.
39. Leonard A. Energy cascade in large eddy simulations of turbulent fluid flows. *Advances in Geophysics* 1974; **18A**:237–248.
40. Bardina J, Ferziger JH, Reynolds WC. Improved turbulence models based on large eddy simulation of homogeneous incompressible turbulent flows. *Report TF-19*, *Thermosciences Division*, Department of Mechanical Engineering, Stanford University, 1983.
41. Pruett CD, Sochacki JS, Adams NA. On Taylor-series expansion of residual stress. *Physics of Fluids* 2001; **13**:2578–2589.
42. Lesieur, M. Staquet C, Le Roy P, Comte P. The mixing layer and its coherence examined from the point of view of two-dimensional turbulence. *Journal of Fluid Mechanics* 1986; **192**:511–534.
43. Drikakis D, Smolarkiewicz PK. On spurious vortical structures. *Journal of Computational Physics* 2001; **172**(1):309–325.

